NOVEMBER 2016 VOL 9 NO 11
www.nature.com/naturegeoscience

nature geoscience

LARGE EARTHQUAKES
Odds rise with the tide

LIFE IN THE TWILIGHT OCEAN
Supported by seasonal pump

COOL EURASIAN WINTERS
Arctic sea ice not implicated

Carbon–climate feedbacks in the late Palaeozoic

LETTERS
PUBLISHED ONLINE: 24 OCTOBER 2016 | DOI: 10.1038/NGEO2822
nature geoscience

Climate, p_{CO_2} and terrestrial carbon cycle linkages during late Palaeozoic glacial–interglacial cycles

Isabel P. Montañez[1*†], Jennifer C. McElwain[2*†], Christopher J. Poulsen[3], Joseph D. White[4], William A. DiMichele[5], Jonathan P. Wilson[6], Galen Griggs[1] and Michael T. Hren[7]

Earth's last icehouse, 300 million years ago, is considered the longest-lived and most acute of the past half-billion years, characterized by expansive continental ice sheets[1,2] and possibly tropical low-elevation glaciation[3]. This atypical climate has long been attributed to anomalous radiative forcing promoted by a 3% lower incident solar luminosity[4] and sustained low atmospheric p_{CO_2} ($\leq$300 ppm)[5]. Climate models[6], however, indicate a CO_2 sensitivity of ice-sheet distribution and sea-level response that questions this long-standing climate paradigm by revealing major discrepancy between hypothesized ice distribution, p_{CO_2}, and geologic records of glacioeustasy[2,6]. Here we present a high-resolution record of atmospheric p_{CO_2} for 16 million years of the late Palaeozoic, developed using soil carbonate-based and fossil leaf-based proxies, that resolves the climate conundrum. Palaeo-fluctuations on the 10^5-yr scale occur within the CO_2 range predicted for anthropogenic change and co-vary with substantial change in sea level and ice volume. We further document coincidence between p_{CO_2} changes and repeated restructuring of Euramerican tropical forests that, in conjunction with modelled vegetation shifts, indicate a more dynamic carbon sequestration history than previously considered[7,8] and a major role for terrestrial vegetation–CO_2 feedbacks in driving eccentricity-scale climate cycles of the late Palaeozoic icehouse.

Atmospheric p_{CO_2} has generally declined over the past half-billion years from highs of several 1,000 ppm, under which early metazoan life radiated, to the lower concentrations characteristic of our pre-industrial glacial state. This trend was markedly disrupted in the Carboniferous–Permian (~360 to 260 million years ago (Ma)) by a sustained period of low p_{CO_2} and increasingly high p_{O_2} attributed to radiation of the Earth's most expansive tropical forests and attendant increased organic matter burial in vast wetland habitats[7,8]. The atypical surface conditions at this time, including anomalously low radiative forcing possibly intensified by high p_{O_2} (ref. 9), strongly influenced the glaciation history and climate and ecosystem dynamics. Large-scale discrepancies, however, between modelled surface conditions and those inferred from geologic records challenge existing climate paradigms and define new paradoxes regarding the climate dynamics of this palaeo-icehouse[1–3,10]. Atmospheric p_{CO_2} estimates, central to resolving these issues, are insufficiently resolved and poorly constrained[5]. Here we develop, for the late Palaeozoic, the first multi-proxy reconstruction of deep-time atmospheric CO_2 at an unprecedented temporal resolution and precision and compare our results with contemporaneous sea level, climate, and tropical vegetation records to assess linkages between climate processes and the role of vegetation–climate feedbacks.

Palaeo-atmospheric p_{CO_2} was reconstructed using soil-formed carbonates and fossil-plant cuticles collected from a series of long-eccentricity (405-kyr) cyclothems in the Illinois Basin, USA (Supplementary Table 1) making the independent CO_2 estimates directly comparable. Cyclothems, which archive glacial–interglacial cycles comparable to the Late Pleistocene[11], provide a chronostratigraphic framework for sampling palaeosols and plant-rich deposits at a 10^3- to 10^4-yr resolution (Supplementary Table 1). Cross-Pangaean correlation of cyclothems enabled the integration of fossil soils from the Appalachian, USA ($n = 16$) and Donets, Ukraine ($n = 4$) basins with the Illinois Basin data ($n = 50$). Pedogenic carbonate and organic matter $\delta^{13}C$ values were applied to the palaeosol CO_2 palaeobarometer using the PBUQ model[12] to fully propagate uncertainty of input parameters and constrain estimated CO_2 uncertainties (see Methods and Supplementary Table 2). Intervals of high palaeosol diversity permitted evaluation of environmental influences on soil-water chemistry and carbonate $\delta^{13}C$. Two plant-based CO_2 proxies, stomatal index (SI)[13] and a mechanistic stomatal model based on a universal leaf-gas-exchange equation[14], complement the mineral-based p_{CO_2} estimates (see Methods). Stomatal frequency and geometry of fossil leaf cuticles and their $\delta^{13}C$ were measured for two genera of long-ranging wetland seed ferns from 13 stratigraphic intervals (Supplementary Table 3). Sampling of isotaphonomic plant-bearing intervals minimized site- and time-specific environmental influences on stomatal and $\delta^{13}C$ values.

Reconstructed CO_2 (Fig. 1) varies between ~200 and 700 ppm with an apparent 10^5-yr rhythmicity. Notably, p_{CO_2} estimates obtained using all three proxies are in good agreement with values falling largely within the uncertainties. Generally, p_{CO_2} falls below the modelled Carboniferous–Permian threshold for glacial inception (560 ppm)[15] and well within the modelled range for sustainability of late Palaeozoic ice sheets[6]. A period mean of 390 ppm $\pm$ 130 ppm (1σ) is double that of existing estimates[5,16] and, considering the 3% lower solar luminosity, is more consistent with the geologic record of ice distribution and magnitudes of glacioeustasy, thus resolving a long-standing data/model mismatch in the behaviour of late Palaeozoic ice sheets[2,3,6]. Late Palaeozoic simulations[6] predict dynamic change in ice-sheet size and distribution for the CO_2 range over which our proxy estimates

[1]Department of Earth and Planetary Sciences, University of California, Davis, California 95616, USA. [2]Earth Institute, School of Biology and Environmental Science, University College Dublin, Belfield, Dublin 4, Ireland. [3]Department of Earth and Environmental Sciences, University of Michigan, Ann Arbor, Michigan 48109, USA. [4]Department of Biology, Baylor University, Waco, Texas 76798, USA. [5]Department of Paleobiology, Smithsonian Museum of Natural History, Washington DC 20560, USA. [6]Department of Biology, Haverford College, Haverford, Pennsylvania 19041, USA. [7]Center for Integrative Geosciences, University of Connecticut, Storrs, Connecticut 06269, USA. [†]These authors contributed equally to this work.
*e-mail: ipmontanez@ucdavis.edu; Jennifer.McElwain@ucd.ie

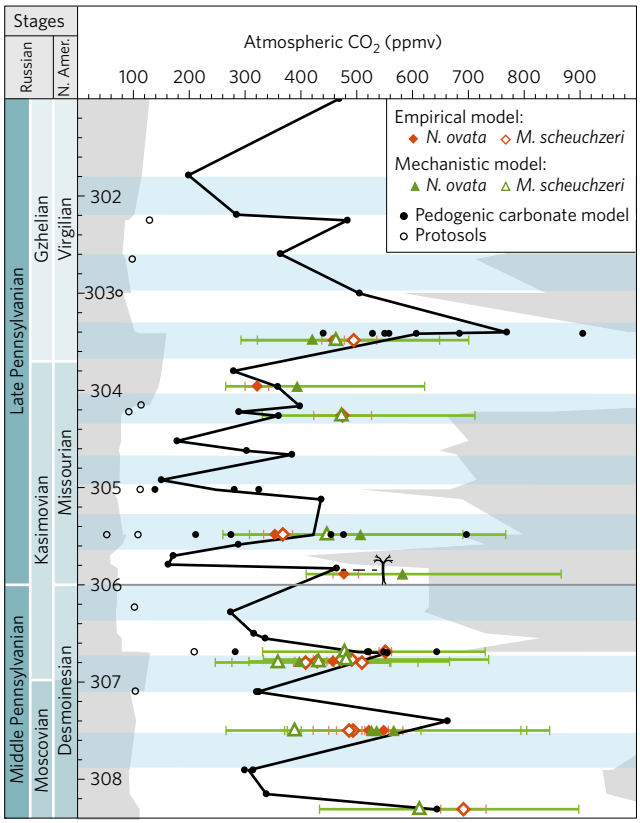

Figure 1 | Pennsylvanian p_{CO_2} reconstructed using pedogenic carbonate- and fossil leaf-based proxies. The trendline connects average values of mineral-based CO_2 estimates per time increment (black filled circles); estimates from Protosols (open circles) are excluded. Grey shading and coloured lines are the 16th and 84th percentile confidence intervals for pedogenic carbonate- and fossil plant-based CO_2 estimates (indicated by green and orange), respectively. Cyclothem series are indicated by alternating blue/white banding (see Supplementary Information for age model). The lycopsid symbol indicates the timing of the MLPB ecologic turnover (~305.9 Ma). *N. ovata, Neuropteris ovata; M. scheuchzeri, Macroneuropteris scheuchzeri.*

fluctuate, with ice distributed in multiple centres and of total volume that matches well with field-based reconstructions[1,10]. Moderate-size ice sheets, which form in simulations using p_{CO_2} between 300 and 600 ppm, are far more sensitive to waxing and waning than the largely unresponsive, coalesced ice sheets predicted under previous CO_2 estimates of <300 ppm, creating magnitudes of glacioeustasy more compatible with geologic records[2].

Timescale (10^5-yr) and magnitude (200 to 300 ppm) of Pennsylvanian p_{CO_2} fluctuations suggest eccentricity-scale variability with CO_2 minima (160 to 300 ppm) comparable to Pleistocene glacial levels[17] but with higher maxima. For those cyclothems subject to highest resolution sampling, CO_2 concentrations rise rapidly early in the cycle, falling to a minimum towards the top of each cycle (Fig. 1). Minimum calculated rates of CO_2 rise (0.001 to 0.005 ppm yr^{-1}) are consistent with the lower range of rates for Pleistocene interglacials (0.003 to 0.02 ppm $yr^{-1} \pm 0.001$ ppm yr^{-1})[17].

Short-term CO_2 fluctuations are superimposed on a 10^6-yr CO_2 trend, which covaries with geologic records of sea level and inferred waxing and waning of ice sheets (Fig. 2). Overall high CO_2 concentrations (540 ppm ± 60 ppm) in the early part of the record (312 to 308.5 Ma) coincide with a long-term stepped eustatic rise and the demise of the main phase of Pennsylvanian glaciation (315 to 311 Ma)[1,2,18], suggesting a CO_2 link to glacial termination. The long-term sea level rise is interrupted by a series of shorter-lived (≤1.5-Myr) lowstands and inferred glaciations[18]. Overall within the age uncertainty, CO_2 rises and falls in-step with major periods of sea level change driven by the retraction and expansion of ice sheets. A particularly acute glaciation (306.5 to 305 Ma; Fig. 2), recognized widely across the middle to late Pennsylvanian boundary (MLPB) by widespread regression and development of particularly prominent incised valleys[11,18,19], coincides with a ~2-Myr period of overall low p_{CO_2} during which time the minima of short-term CO_2 fluctuations dip below 300 ppm and progressively decrease to a CO_2 nadir of <200 ppm. The subsequent rise in p_{CO_2} to a late Pennsylvanian apex (303.4 Ma) heralds peak transgression (O7 on Fig. 2), which demarks the end of the long-term stepped eustatic rise and waning of ice sheets through the latter half of the Pennsylvanian. The subsequent p_{CO_2} drop at the close of the Carboniferous to sustained low earliest Permian values (Fig. 2) is coincident with a globally recognized major eustatic fall[18,20] and the hypothesized early Permian apex of late Palaeozoic glaciation[1,3,10].

We document a coincidence in timing between CO_2 fluctuations and major floral community turnovers within the Pennsylvanian tropical forests that invokes a potential role for CO_2-forcing indirectly via changes in hydroclimate and possibly directly through the impact of 'CO_2 starvation' on plant ecophysiology. At the eccentricity scale and contemporaneous with the 10^5-yr rhythmicity in p_{CO_2}, repeated shifts in the tropical lowlands occurred between glacial floras characteristic of swamp habitats (for example, Lepidodendrales (lycopsids) and Medullosales) and interglacial seasonally dry floras (for example, tree ferns, conifers, Cordaitales and Medullosales)[21]. Intense short-lived MLPB glaciation on the heels of longer-term warming and drying, involved abrupt vegetation turnover with loss of most lycopsids throughout the Euramerican palaeotropics and stepped emergence of more water-stress-tolerant tree ferns as the swamp-community dominants[21,22]. The timing of this major restructuring (305.8 Ma) during overall declining p_{CO_2} and a drop in short-term CO_2 fluctuations below 300 ppm (black trendline, Fig. 1) suggests ecologic turnover at a CO_2 threshold. The widespread contraction of the humid tropical forests and expansion of xerophytic woodland and scrub vegetation[23] that followed led to habitat fragmentation and resource restriction, which in turn accelerated amphibian extinction rates and reptile diversification creating strong endemism[24]. A subsequent permanent shift in tropical Euramerica to dominance of seasonally dry flora and extreme habitat restriction of wetland plants occurred across the Carboniferous–Permian boundary[23,25] synchronous with the drop in p_{CO_2} to a sustained nadir (<200 ppm).

Major restructuring of wetland forests was undoubtedly influenced by shifts to seasonally dry conditions during eccentricity-scale interglacials[21] and longer-term aridification beginning in the middle Pennsylvanian and intensifying through the early Permian[23,25]. Given the conjunction of ecologic turnovers and low-CO_2 'deep glacials', we hypothesize that the very low atmospheric p_{CO_2} and high p_{O_2} at these times could have differentially affected the physiological response of terrestrial plant groups, thereby influencing their ecological competitiveness. Terrestrial carbon cycle models[26] document the potential detrimental impact of this unique atmospheric gas composition on vascular plant functioning—a pattern that is reversed at $p_{CO_2} > 400$ ppm. On the basis of theoretical[27] and experimental[28] grounds, and in the absence of any specialized carbon-concentrating mechanisms, high O_2/CO_2 could have differentially affected the gas-exchange capacity, photosynthetic physiology, and water-use efficiency (WUE; carbon assimilation relative to transpiration water loss) of plant groups.

To test this further, palaeo-WUE of six taxonomic groups representing species that dominated the ecosystems during the

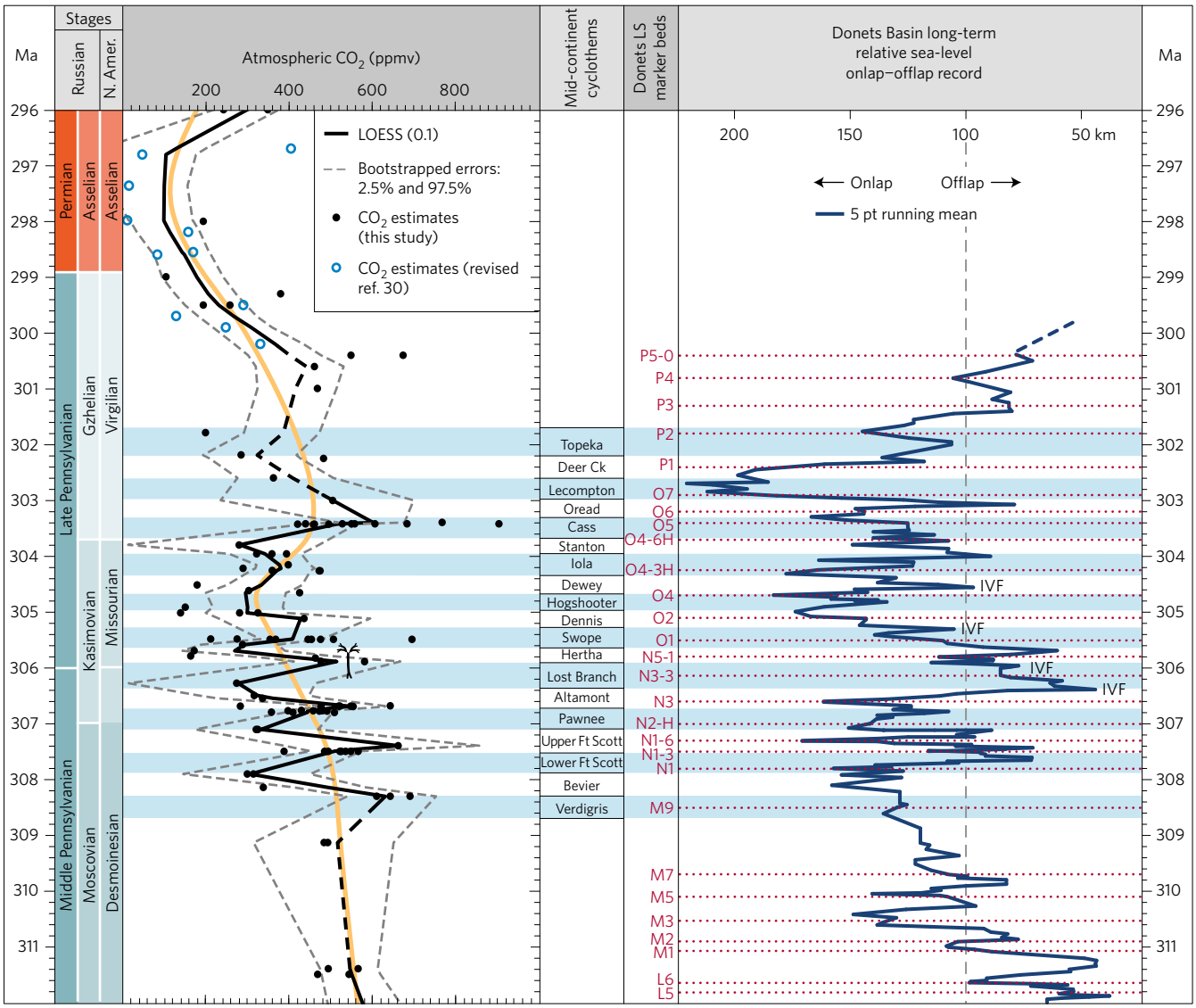

Figure 2 | Consensus p_{CO_2} curves defined by LOESS analysis of combined pedogenic carbonate- and fossil plant-based CO_2 estimates. LOESS CO_2 estimates (black filled circles) include CO_2 estimates (open blue circles) from ref. 30 revised using MatLab code PBUQ[12] and improved input parameters. LOESS trend lines are 0.1 (black) and 0.3 (orange) smoothing. Donets Basin sea-level history[18] was revised for the newest Carboniferous timescale; major sea-level lowstands are intervals of offlap beyond 100 km (dashed line). Interbasinal correlation of cyclothems is indicated by alternating blue and white intervals. Incised valley fill (IVF): location of 'major' incised valley fills recording the greatest extents of seaward withdrawal of the Midcontinent Sea[11,19]. The lycopsid symbol is as in Fig. 1. LS, Limestone.

period of study were modelled using a terrestrial biosphere model and Pennsylvanian–Permian O_2/CO_2 (Fig. 3a and see Supplementary Information). WUE of fossil tree ferns (for example, *Pecopteris*) was consistently >5.5 times higher than coeval Lepidodendrales, whereas *Macroneuropteris* and 'other Medullosales' were minimally 2.5 to 3 times greater (Fig. 3b). The 'WUE advantage' of Medullosales over Lepidodendrales increased further when prevailing atmospheric CO_2 decreased below 400 ppm (Fig. 3b), characteristic of the 'deep palaeo-glacials'. Although these ecophysiological findings suggest that climatic/edaphic drying would have been ecologically disadvantageous to Lepidodendrales and *Sphenophyllum* compared with all other taxa across the range of estimated Pennsylvanian–Permian CO_2 concentrations, they further strongly implicate the role of a low CO_2-threshold (<400 ppm) as a driver of ecological turnovers.

Climate-driven vegetation changes had the potential to feedback on CO_2 through changes in terrestrial C sequestration given the expanse and predominance of the tropical forests[8] during glacials and their dynamic compositional changes[21,23]. At the eccentricity scale, modelled biome distribution[6] in response to orbitally driven changes in solar insolation and p_{CO_2} indicates a large displacement in tropical vegetation (up to 7%) with shifts from wetland forests to seasonally dry flora during interglacials (Supplementary Table 9), a finding consistent with palaeobotanical records[21]. Estimated consequent changes in C sequestration potential are sufficient to increase the CO_2 flux to the atmosphere by 0.3 ppm $yr^{-1} \pm$ 0.2 during interglacials and reduce it by a similar amount during longer-lived glacials. Even accounting for CO_2 absorption by other surface C sinks, the increased CO_2 flux substantially outpaces minimum CO_2 rise rates during deglaciation inferred from our record, demonstrating the potential for tropical vegetation to modulate late Palaeozoic p_{CO_2}. Additionally, rapid tundra expansion (by up to 16%), coincident with solar insolation minima at the end of each interglacial, indicates a possible carbon sink of 0.02 to 0.05 ppm yr^{-1}, highlighting the potential role of high-latitude vegetation in promoting renewed ice buildup.

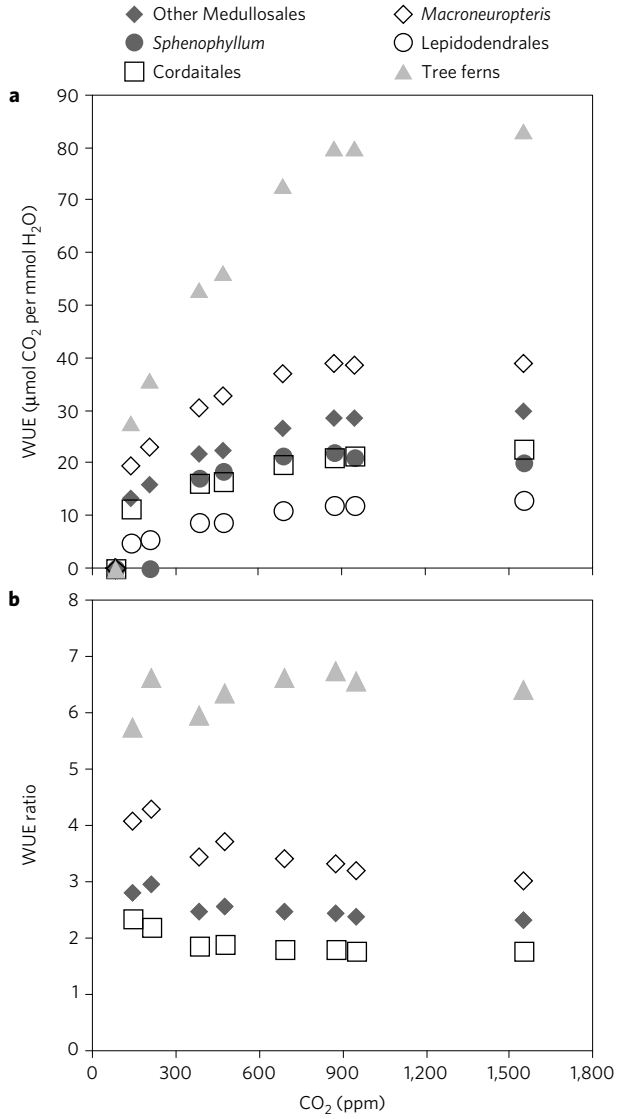

Figure 3 | Comparison of modelled water-use efficiency (WUE) of dominant Carboniferous taxa in relation to prevailing atmospheric p_{CO_2} concentration. a,**b**, WUE values modelled using BIOME—BGC v.4.2 (see Supplementary Information) (**a**), and expressed as a ratio to the WUE values of Lepidodendrales (**b**). Note that tree ferns consistently have WUE values that are higher than all other taxa and at minimum six times greater that those of Lepidodendrales, whereas the *Macroneouropteris*/Lepidodendrales WUE ratio shows an increasing trend with declining atmospheric CO_2.

This first multi-proxy CO_2 record for the pre-Cenozoic illustrates substantial fluctuation in palaeo-atmospheric p_{CO_2} over a hierarchy of timescales during the only other Phanerozoic period of overall low CO_2. Notably, Pennsylvanian CO_2 fluctuations, within the range anticipated for the twenty-first century, were associated with major changes in ice volume, sea level and repeated restructuring of the Earth's most extensive tropical forests. In stark contrast to the Late Pleistocene when the terrestrial organic carbon reservoir served as a C sink during interglacials[29], a net positive terrestrial C sink was established during late Palaeozoic glacials due to the unprecedented geographic expanse and carbon sequestration potential of the palaeo-tropical wetland forests. Together, the response to climate change of the C sequestration potential of tropical and tundra biomes, extending over 35 to 50% of Pangaea, highlights the capacity of the terrestrial biosphere to drive C cycle dynamics during Earth's penultimate icehouse. Notably, the very low p_{CO_2} of the deep glacials raises an important yet unaddressed ecologic issue as to whether selective ecophysiological stress at CO_2 thresholds contributed to major ecologic turnovers of the earliest tropical forests.

Methods

Methods, including statements of data availability and any associated accession codes and references, are available in the online version of this paper.

Received 11 May 2016; accepted 7 September 2016; published online 24 October 2016

References

1. Fielding, C. R. *et al*. Stratigraphic imprint of the Late Palaeozoic Ice Age in eastern Australia: a record of alternating glacial and nonglacial climate regime. *J. Geol. Soc. Lond.* **165,** 129–140 (2008).
2. Montañez, I. P. & Poulsen, C. J. The Late Paleozoic Ice Age: an evolving paradigm. *Annu. Rev. Earth Planet. Sci.* **41,** 629–656 (2013).
3. Soreghan, G. S., Sweet, D. E. & Heavens, N. G. Upland glaciation in tropical Pangaea: geologic evidence and implications for late Paleozoic climate modeling. *J. Geol.* **122,** 137–163 (2014).
4. Crowley, T. J. & Baum, S. K. Modeling late Paleozoic glaciation. *Geology* **20,** 507–510 (1992).
5. Royer, D. L. *Treatise on Geochemistry* 2nd edn, Vol. 6 (eds Holland, H. & Turekian, K.) 251–267 (Elsevier Ltd, 2014).
6. Horton, D. E., Poulsen, C. J. & Pollard, D. Influence of high-latitude vegetation feedbacks on late Palaeozoic glacial cycles. *Nat. Geosci.* **3,** 1–6 (2010).
7. Berner, R. A. The long-term carbon cycle, fossil fuels, and atmospheric composition. *Nature* **426,** 323–326 (2003).
8. Cleal, C. J. & Thomas, B. A. Palaeozoic tropical rainforests and their effect on global climates: is the past the key to the present? *Geobiology* **3,** 13–31 (2005).
9. Poulsen, C. J., Tabor, C. & White, J. D. Long-term climate forcing by atmospheric oxygen concentrations. *Science* **348,** 1238–1241 (2015).
10. Isbell, J. *et al*. Glacial paradoxes during the late Paleozoic ice age: evaluating the equilibrium line altitude as a control on glaciation. *Gondwana Res.* **22,** 1–19 (2012).
11. Heckel, P. H. Pennsylvanian stratigraphy of Northern Midcontinent Shelf and biostratigraphic correlation of cyclothems. *Stratigraphy* **10,** 3–39 (2013).
12. Breecker, D. O. Quantifying and understanding the uncertainty of atmospheric CO_2 concentrations determined from calcic paleosols. *Geochem. Geophys. Geosyst.* **14,** 3210–3220 (2013).
13. McElwain, J. C. & Chaloner, W. G. Stomatal density and index of fossil plants track atmospheric carbon dioxide in the palaeozoic. *Ann. Bot.* **76,** 389–395 (1995).
14. Franks, P. J. *et al*. New constraints on atmospheric CO_2 concentration for the Phanerozoic. *Geophys. Res. Lett.* **41,** 4685–4694 (2014).
15. Lowry, D. P., Poulsen, C. J., Horton, D. E., Torsvik, T. H. & Pollard, D. Controls on Paleozoic ice sheet initiation. *Geology* **42,** 627–630 (2014).
16. Breecker, D. O., Sharp, Z. D. & McFadden, L. D. Atmospheric CO_2 concentrations during ancient greenhouse climates were similar to those predicted for A.D. 2100. *Proc. Natl Acad. Sci. USA* **107,** 576–580 (2010).
17. Siegenthaler, U. *et al*. Stable carbon cycle-climate relationship during the Late Pleistocene. *Science* **310,** 1313–1317 (2005).
18. Eros, J. M. *et al*. Sequence stratigraphy and onlap history, Donets Basin, Ukraine: Insight into Late Paleozoic ice age dynamics. *Palaeogeogr. Palaeoclimatol. Palaeoecol.* **313,** 1–25 (2012).
19. Belt, E. S., Heckel, P. H., Lentz, L. J., Bragonier, W. A. & Lyons, T. W. Record of glacial-eustatic sea-level fluctuations in complex middle to late Pennsylvanian facies in the Northern Appalachian Basin and relation to similar events in the Midcontinent basin. *Sediment. Geol.* **238,** 79–100 (2011).
20. Koch, J. T. & Frank, T. D. The Pennsylvanian-Permian transition in the low-latitude carbonate record and the onset of major Gondwanan glaciation. *Palaeogeogr. Palaeoclimatol. Palaeoecol.* **308,** 362–372 (2011).
21. DiMichele, W. A. Wetland-dryland vegetational dynamics in the Pennsylvanian ice age tropics. *Int. J. Plant Sci.* **175,** 123–164 (2014).
22. Phillips, T. L. & Peppers, R. A. Changing patterns of Pennsylvanian coal-swamp vegetation and implications of climatic control on coal occurrence. *Int. J. Coal Geol.* **3,** 205–255 (1984).

23. DiMichele, W. A., Montañez, I. P., Poulsen, C. J. & Tabor, N. J. Vegetation-climate feedbacks and regime shifts in the Late Paleozoic ice age earth. *Geobiology* **7,** 200–226 (2009).
24. Sahey, S., Benton, M. J. & Falcon-Lang, H. J. Rainforest collapse triggered carboniferous tetrapod diversification in Euramerica. *Geology* **38,** 1079–1082 (2010).
25. Tabor, N. J., DiMichele, W. A., Montañez, I. P. & Chaney, D. S. Late Paleozoic continental warming of a cold tropical basin and floristic change in western Pangea. *Int. J. Coal Geol.* **119,** 177–186 (2013).
26. Beerling, D. J. & Berner, R. A. Impact of a Permo-Carboniferous high O_2 event on the terrestrial carbon cycle. *Proc. Natl Acad. Sci. USA* **97,** 12428–12432 (2000).
27. Flexas, J. Mesophyll diffusion conductance to CO_2: an unappreciated central player in photosynthesis. *Plant Sci.* **193,** 70–84 (2012).
28. McElwain, J. C., Yiotis, C. & Lawson, T. Using modern plant trait relationships between observed and theoretical maximum stomatal conductance and vein density to examine patterns of plant macroevolution. *New Phytol.* **209,** 94–103 (2015).
29. Adams, J. M., Faure, H., Faure-Denard, L., McGlade, J. M. & Woodward, F. I. Increases in terrestrial carbon storage from the Last Glacial Maximum to the present. *Nature* **348,** 711–714 (1990).
30. Montañez, I. P. *et al*. CO_2-forced climate instability and linkages to tropical vegetation during late paleozoic deglaciation. *Science* **315,** 87–91 (2007).

Acknowledgements

We thank D. Breecker for discussion and comments on this work, and R. Barclay, J. Antognini, D. Garello, A. Byrd, R. Chen, C. Marquardt and D. Rauh for assistance in the research, D. Horton for access to palaeoclimate model results, and N. Tabor for a subset of stable isotopic analyses. This work was funded by NSF grants EAR-1338281 (I.P.M.), EAR-1338200 (C.J.P.), EAR-1338247 (J.D.W.), and EAR-1338256 (M.T.H.), and ERC-2011-StG and 279962-OXYEVOL to J.C.M.

Author contributions

I.P.M. and J.C.M. devised and carried out the CO_2 proxy reconstruction and J.D.W., W.A.D., J.P.W. and M.T.H. contributed to the parameterization and sensitivity analyses of the palaeo-CO_2 models. C.J.P. undertook the climate modelling analysis, J.D.W. the biogeochemical ecosystem modelling, and G.G. contributed to the CO_2 modelling. All authors contributed to the development of ideas, data interpretation, and writing of the manuscript.

Additional information

Supplementary information is available in the online version of the paper. Reprints and permissions information is available online at www.nature.com/reprints. Correspondence and requests for materials should be addressed to I.P.M. or J.C.M.

Competing financial interests

The authors declare no competing financial interests.

Methods

Samples. Calcite nodules and rhizolith samples ($n = 304$) were collected from Pennsylvanian-age cyclothemic successions from: Illinois Basin surface and subsurface mines and five cores, housed at the Prairie Research Institute, Illinois State Geological Survey; and outcrops in the Appalachian Basin, USA and Donets Basin, Ukraine (Supplementary Table 2). Fossil pteridosperm leaves were extracted from samples obtained from the Department of Paleobiology, National Museum of Natural History, Smithsonian Institution (Supplementary Table 3). For outcrops, profiles were trenched to ensure a fresh exposure; samples were collected from at least 0.5 m beneath the surfaces of mature and immature (Protosols) palaeosols. Palaeosols were classified on the basis of macro- and micromorphologic features using the scheme of ref. 31. Cuticles of individual pinnules were isolated from bedding plane surfaces either by the non-destructive (polyester peels) technique of ref. 32 or by bulk maceration.

Geochemical methodology. Pedogenic carbonate samples were thick-sectioned (~200 μm thick) and evaluated for evidence of recrystallization or diagenetic cements using transmitted and cathodoluminescent light (see ref. 33). Micritic calcite exhibiting pedogenic micromorphologies was microsampled using a Merchantek automated microsampler. Approximately 50 μg of carbonate was roasted at 375 °C under vacuum for 2 h to remove organics and subsequently reacted in 105% phosphoric acid at 90 °C in a common acid bath of a GVI Optima IRMS in the Stan Margolis Stable Isotope Laboratory, University of California, Davis (UCD). External precision for $\delta^{13}C$ measurements based on standards and replicates was $>\pm 0.04‰$.

Organic matter C isotopic data were obtained from: coal vitrinite macerals and discrete fossil plant matter in mudstones closely associated with palaeosols; and/or from organic matter occluded within pedogenic nodules. For CO_2 estimates made using the mechanistic model of ref.14, the $\delta^{13}C$ of fossil leaf cuticles, which were used for stomatal-index-based CO_2 estimates, was measured. The $\delta^{13}C$ values of all materials are presented in Supplementary Tables 2 and 3.

For coals and sediment-associated organic matter, samples were rinsed in 1 N HCl overnight at room temperature and washed four times with nanopure H_2O to remove any carbonate and hydrolysable C. Between one hundred and two hundred micrograms of cleaned and dried organic matter or fossil cuticle, previously cleaned to remove mineral matter, were loaded in tin capsules. C isotope analysis of coals, discrete fossil plant matter, and fossil cuticles was carried out on a PDZ Europa elemental analyser interfaced to a PDZ Europa 20-20 IRMS at the Stable Isotope Facility, UCD. External precision for the $\delta^{13}C$ measurements based on repeated analysis of standards is better than $\pm 0.3‰$. Additionally, the $\delta^{13}C$ values of organic matter occluded within pedogenic carbonates ($n = 22$) were measured for 18 stratigraphic intervals. Organic matter was isolated from 10 to 20 mg of pulverized carbonate through repeated rinsing with 1 N HCl and subsequently washed with nanopure H_2O to remove all carbonate. Dry residues were processed offline and analysed by IRMS in the UC Davis Stable Isotope Laboratory or in the Stable Isotope Laboratory, Southern Methodist University (courtesy of N. Tabor). External precision for the $\delta^{13}C$ measurements is $\leq \pm 0.3‰$.

Input parameters for palaeosol barometer model and uncertainty estimates. The MatLab code PBUQ[12] was used to estimate palaeo-CO_2. PBUQ uses the palaeosol carbonate CO_2 palaeobarometer equation[34] and Monte Carlo error propagation to define a distribution of CO_2 from which mean, median and percentile (16th and 84th) values are calculated. Individual input data for the PBUQ model ($n = 81$) consist of average measured values from either: an individual palaeosol of a given soil order (that is, a sample); or a series of stacked palaeosols of the same soil order from within one stratigraphic interval (that is, a sample set). Palaeosols of the same age but of differing soil order were modelled individually resulting in multiple estimates for over 60% of the time slices. Input parameters for PBUQ were calculated as follows and are presented in Supplementary Table 2.

Temperature. PBUQ uses, as a default, palaeo-MAAT to calculate the temperature of soil carbonate formation based on a transfer function ($Y = 0.506 * X + 17.974$, where Y is the carbonate formation temperature and X is MAAT)[12]. For the subset of new samples ($n = 70$) of Pennsylvanian through earliest Permian age, we assigned a constant MAAT range (23 °C ± 3 °C) that spans the minimum to maximum temperatures modelled for the late Palaeozoic continental tropics over a p_{CO_2} of 280 to 840 ppm (refs 2,6). This approach conservatively represents late Palaeozoic MAATs in the palaeotropics. The temperature range utilized in this study (20 to 26 °C) overlaps with the lower range of soil temperatures (22 to 32 °C) inferred from pedogenic minerals[35] for four of the same stratigraphic intervals in the Illinois Basin, thus providing confidence that a MAAT range of 20 to 26 °C is reasonable. Proxy soil temperatures could be several degrees to possibly 10 °C higher than warm-season surface air temperatures during the Pennsylvanian and early Permian given the influence of surface latent and sensible heat fluxes on soil temperatures[36,37]. Notably, if the MAAT values used in this study are too low (that is, if surface air temperatures in the tropics averaged annually over 26 °C) then the CO_2 estimates during peak intervals shown on Figs 1 and 2 are underestimated and the magnitudes of change within the 10^5-yr fluctuations are minimum ranges. Comparison of CO_2 estimates made using the same parameterization of PBUQ but with a temperature of 32 °C ± 3 °C indicates an average difference of 42.4 ppm between the higher temperature estimates and those made using 23° C ± 3 °C and a standard deviation of the variance of ± 147.3 ppm. These values fall within the uncertainty of modelled p_{CO_2}.

For the modelling of previously published[30] latest Pennsylvanian to early Permian sample sets ($n = 11$), we constrained MAATs using proxy soil temperatures[25], which were derived from many of the same palaeosols (~50%) used in this study. See Supplementary Table 2 for specifics of how MAATs were constrained for this subset of samples.

Total soil CO_2 $\delta^{13}C$. The average (±2 standard error (s.e.)) $\delta^{13}C$ values of pedogenic carbonates from a given palaeosol or series of palaeosols was used as a proxy for the $\delta^{13}C$ value of total soil CO_2. We consider measured pedogenic carbonate $\delta^{13}C$ values to be a robust proxy of soil-water CO_2 during formation given the lack of evidence for mineral recrystallization and overgrowth and the moderate burial thermal histories of the Illinois Basin[35].

Respired $\delta^{13}C$. PBUQ permits four options for defining the $\delta^{13}C$ value of the respired CO_2 contribution to the soil. This study utilized two of these options. The first proxy of respired $CO_2\delta^{13}C$ is the average (±2 s.e.) measured $\delta^{13}C$ of coal macerals and fossil plant matter extracted from mudstones most stratigraphically proximal to the carbonate-bearing palaeosols. In the cyclothemic successions of the Illinois, Appalachian and Donets basins, coals and/or plant-rich mudstones typically overlie palaeosols; thus, the organic matter is considered representative of the organic-rich surface A horizon of these palaeosols. The second proxy of respired $CO_2\delta^{13}C$ is the measured $\delta^{13}C$ value of organic matter occluded within pedogenic carbonates, which formed in the B horizon of palaeosols. For those soils for which CO_2 estimates were obtained using both proxies of respired $CO_2\delta^{13}C$, p_{CO_2} estimates shown on Figs 1 and 2 are those made using occluded organic matter. This choice reflects that organic matter occluded in the pedogenic carbonates most closely approximates that of the soil in which the carbonate formed. CO_2 estimates for both proxies of soil-respired $CO_2\delta^{13}C$ are provided in Supplementary Table 2.

PBUQ makes a correction to the input $\delta^{13}C_{org}$ values of +0.5‰ for organic matter that formed in the A horizon and of −1‰ for that formed in the B horizon. This correction is to account for the contribution in the carbonate-forming horizon of respired CO_2 from A and B horizons of which the former is ^{12}C-enriched relative to the latter. In this study, although the $\delta^{13}C$ values of the coal macerals are representative of the A horizon, a +0.5‰ correction was not applied to coal $\delta^{13}C_{org}$ values given processes that can lead to ^{13}C-enrichment in coal relative to soil organic matter in the A horizon. The $\delta^{13}C$ of coals rich in macerals derived from woody tissues (vitrinite) are ^{13}C-enriched (~2‰) relative to macerals derived from lipid-rich precursor material (liptinites)[38]. Therefore, the respired CO_2 in the A horizon of palaeosols, which would have been dominated by respiration of leaf material and other less refractory organic matter, was probably ^{13}C-depleted relative to the organic matter contained in vitrinite-rich coals; thus, the correction is effectively already accounted for. Moreover, coal $\delta^{13}C$ typically increases during coalification resulting in values up to ~1‰ higher than contemporaneous C_3-type terrestrial plants[38]. Additionally, no correction was made to the input $\delta^{13}C_{org}$ values of occluded organic matter, which formed in the B horizon, given that occluded organic matter $\delta^{13}C$ values measured in this study were similar to, to slightly more negative than, those of contemporaneous coal or fossil plant matter.

Atmospheric $\delta^{13}C$. The best estimates of marine $\delta^{13}C_{calcite}$ ($\pm 1\sigma$) from a global compilation of Permo-Carboniferous brachiopods[39] were input to PBUQ, from which $\delta^{13}C_{atm}$ is calculated using the input temperatures and the temperature-sensitive $\varepsilon_{calcite-CO2(g)}$ equation of ref. 40.

Soil-respired CO_2, $S(z)$. The soil-order specific ranges of soil-respired CO_2 concentration ($S(z)$), which were defined on a set of 130 Holocene carbonate-bearing palaeosols[41], and modified in ref. 12, were used in the PBUQ modelling.

Reported p_{CO_2} estimates (Supplementary Table 2) are presented as interquartile mean values rather than the default median values given that the truncated mean is a robust estimator of centrality for mixed distributions and the skewed $S(z)$ input data set. A full discussion of this statistical approach and comparison of the median and interquartile mean values of best estimates of late Palaeozoic p_{CO_2} are presented in the Supplementary Information and Supplementary Fig. 4.

Fossil cuticle-based CO_2 estimates. Palaeo-atmospheric p_{CO_2} was further estimated using two long-ranging and isotaphonomic, wetland pteridosperms (*Neuropteris ovata* and *Macroneuropteris scheuchzeri*) applied to the SI method and a mechanistic stomatal model of p_{CO_2}. Measured input parameters for both proxy methods and the resulting p_{CO_2} estimates are presented in Supplementary Table 3.

Stomatal index method. The stomatal density and index of abaxial cuticles were measured on macrofossil cuticle specimens (peels) or on fragments obtained through bulk maceration. A strong inverse relationship between stomatal density (SD) or SI and atmospheric CO_2 concentration has been documented in living and extant plants[13,42,43]. Comparison of SI estimates and temporal trends between coexisting extant and extinct plants further demonstrates the robustness of this CO_2 proxy[44,45]. SD, the number of stomata per square millimetre area, and SI, the percentage of leaf epidermal cells that are stomatal, were measured using epifluorescent microscopy and a Leica 'stacked image' capture and analysis system. Between 4 and 10 regions (0.04 mm^2) were counted for each cuticle/leaf fragment to define mean values per leaf (see ref. 44). We use the SI measurements as proxies of palaeoatmospheric CO_2 given that SI is generally considered a better metric of changes in atmospheric CO_2 because it is less affected by environmental conditions than SD[42,46]. As some studies have suggested that SI can be impacted by environmental factors other than p_{CO_2} (for example, irradiance, nutritional constraints[47,48]), we characterized, for leaf fragments of individual plants, the natural intra- and inter-pinnule variability in stomatal traits.

SI values of medullosan (seed fern) cuticles from 13 Pennsylvanian cyclothems (Illinois Basin) indicate a lack of species specificity and an intra- and inter-pinnule variability within individual plant beds (0.4 to 1.6, respectively) that is much less than the temporal variability (Supplementary Fig. 2). Within the limits of the data distribution, both taxa and the variants define similar temporal shifts in SI that are beyond the natural intra- and inter-pinnule and geographic variability. We interpret the similar temporal changes in SI indicated by all taxa to record an atmospheric CO_2 driver to the long-term genotypic response of SI in these Pennsylvanian plants.

SI values were calibrated to palaeo-p_{CO_2} for a given time increment using the nearest-living equivalent (NLE) method of ref. 49, as applied to tree ferns[50], and the stomatal ratio method[13]. Two extant tree ferns in the Order Cyatheales (*Cyathea cooperii*: SI = 18.0; *Dicksonia antarctica*: SI = 20) and one tree-fern-like fern (*Todea barbara* (Osmundales): SI = 16.2) were selected as potential NLE species (NLEs) for the taxa *Neuropteris* and *Macroneuropteris*. Selection was based on similarities in overall vegetative and ecological traits, which determine ecophysiological processes, rather than reproductive traits, which differ between ferns and seed ferns. The traits used included pinnae and pinnule macro- and micromorphology and ecological traits such as canopy position and relative abundance within palaeo- and modern forest communities (all understory, typically sub-dominant but can be dominant). An average SI value for the three NLEs of 18.07 was used to calculate the stomatal ratio (NLE SI/Fossil SI) from which CO_2 concentration was estimated using the recent standardization according to the formula of ref. 13 below:

$$\text{Palaeo-}p_{CO_2}\,(\text{ppm}) = ((\text{SI}_{\text{NLEs}} = 18.066)/\text{SI}_{\text{fossil}})$$

$$\times 360\,\text{ppm}\ [\text{Recent standardization}]$$

The Carboniferous standardization of ref. 49, frequently used to estimate maximum CO_2, was not used here because it assumes that geochemical mass balance model estimates of p_{CO_2} for the Carboniferous are correct and anchors subsequent stomatal ratio-based CO_2 estimates to this Carboniferous calibration point. Such an approach would not be valid here where we aim to quantify Carboniferous CO_2 independently of any model-based estimates.

Mechanistic model. The measured stomatal traits (density and guard cell length and width) and cuticle $\delta^{13}C$ values of the two seed fern taxa used in this study were applied to the mechanistic stomatal model of ref. 14. This approach based on the universal leaf-gas-exchange equation, equates atmospheric CO_2 with CO_2 assimilation rate (A_n), which is prescribed at the taxonomic level; total stomatal conductance of the leaf, which is inferred from fossil cuticle stomatal traits; and the difference in concentration of CO_2 between the atmosphere and in the leaf (Ci/Ca ratio). Scaling factors used in the mechanistic model are a combination of measured and inferred values (Supplementary Table 4). In this study, the stomatal traits (density and guard cell length) of the abaxial surface of the cuticles were measured on epifluorescent 'stacked image' photographs of cuticle/leaf fragments to define mean values per leaf. Only the abaxial cuticle surface was measured as these seed fern taxa were hypostomatous.

CO_2 estimates made using this mechanistic model are sensitive to the input parameters of photosynthetic rate (A_o), defined in ref. 14 as that under current ambient CO_2 conditions (400 ppm), and total operational conductance to CO_2 diffusion from the atmosphere to sites of photosynthesis in the leaf ($g_{c(tot)}$). Notably, CO_2 estimates vary by several hundreds of parts per million depending on which values are prescribed[51]. Ref. 14 suggest a photosynthetic rate (A_o) for all seed ferns (pteridosperms, including medullosans) of 6 μmol CO_2 m^{-2} s^{-1} using a modern gymnosperm NLE. On the basis of all other physiological traits of these medullosans (high xylem conductivity, high g_{max}, relatively high vein density, thin cuticle and broad, thin leaves), an angiosperm or tropical fern model is deemed more appropriate[46]. Thus, A_o values (μmol m^{-2} s^{-1}) for the two seed ferns studied were estimated using three approaches: the scaling relationship between vein density (D_v) and A_o for a range of angiosperm and fern taxa from refs 28,52); estimated K_{leaf} using measurements of mesophyll path length compared with a modern data set of ref. 53; and ecosystem model constraints (BIOME-BGC v.4.2)[54] on canopy average and maximum sunlit canopy CO_2 assimilation under 400 ppm and the range of hypothesized late Palaeozoic p_{O_2}. The methodology for these three approaches and results are presented in refs 51,55.

Total operational conductance ($g_{c(tot)}$) is based on leaf boundary layer conductance (g_{cb}) to CO_2, the mesophyll conductance (g_m), and operational stomatal conductance ($g_{c(op)}$). The suggested values of ref. 14 were used for g_{cb} and g_m. Ref. 14 recommends a scaling factor a 0.2 from maximum conductance to CO_2 ($g_{c(max)}$) to $g_{c(op)}$. This scaling relationship, however, is inversely correlated with CO_2 (ref. 56). Both ref. 56 and ref. 28 observe a slightly higher scaling relationship for $g_{c(op)}/g_{c(max)}$ of 0.25 and 0.3 respectively. *Neuropteris* and *Macroneuropteris* occupied ecological habitats with high water availability and could potentially have achieved 40% of $g_{c(max)}$ values (0.4 scaling). A sensitivity analysis of values ranging from 0.2 to 0.4 was undertaken to account for varying water supply rates to leaf tissue and site water availability and thus uncertainty in this parameter[51] but the most conservative value of 0.2 was used here.

Details regarding the age (Supplementary Table 1) and geologic (Supplementary Fig. 9) models used in this study, statistical analysis of the p_{CO_2} estimates, the terrestrial ecosystem modelling (BIOME-BGC v.4.2), and the terrestrial carbon sequestration calculations and associated discussion are presented in the Supplementary Information.

Code availability. The code used to generate the pedogenic carbonate-based p_{CO_2} estimates can be assessed in ref. 12. The code used to generate the mechanistic stomatal-based p_{CO_2} estimates can be assessed in ref. 14. The code for the terrestrial biosphere modelling can be downloaded free of charge at http://www.ntsg.umt.edu/project/biome-bgc. The GENESIS Earth system climate model, v. 3.0, coupled to dynamic ecosystem and ice-sheet modelling components was used to generate the modelled vegetation data in Supplementary Table 9 (refs 57–59).

Data availability. All data supporting the findings of this study are available in the Supplementary Information files. Any additional information regarding this study is available from the corresponding author on request.

References

31. Mack, G. H., James, W. C. & Monger, H. C. Classification of paleosols. *Geol. Soc. Am. Bull.* **105,** 129–136 (1993).
32. Kouwenberg, L. L. R., Hines, R. R. & McElwain, J. C. A new transfer technique to extract and process thin and fragmented fossil cuticle using polyester overlays. *Rev. Palaeobot. Palynol.* **145,** 243–248 (2007).
33. Deutz, P., Montañez, I. P. & Monger, H. C. Morphologies and stable and radiogenic isotope compositions of pedogenic carbonates in Late Quaternary relict and buried soils, New Mexico: an integrated record of pedogenic overprinting. *J. Sediment. Res.* **72,** 809–822 (2002).
34. Cerling, T. E. Use of carbon isotopes in paleosols as an indicator of the pCO_2 of the paleoatmosphere. *Glob. Geochem. Cycles* **6,** 307–314 (1992).
35. Rosenau, N. A. & Tabor, N. J. Oxygen and hydrogen isotope compositions of paleosol phyllosilicates: differential burial histories and determination of middle-late Pennsylvanian low-latitude terrestrial paleotemperatures. *Palaeogeol. Palaeoclimatol. Palaeoecol.* **392,** 382–397 (2013).
36. Passey, B. H., Levin, N. E., Cerling, T. E., Brown, F. H. & Eiler, J. M. High-temperature environments of human evolution in East Africa based on bond-ordering in paleosol carbonates. *Proc. Natl Acad. Sci. USA* **107,** 11245–11249 (2010).
37. Quade, J., Eiler, J., Daeron, M. & Achyuthan, H. The clumped isotope geothermometer in soil and paleosol carbonate. *Geochim. Cosmochim. Acta* **105,** 92–107 (2013).
38. Rimmer, S. M., Rowe, H. D., Taulbee, D. N. & Hower, J. C. Influence of maceral content on $\delta^{13}C$ and $\delta^{15}N$ in a Middle Pennsylvanian coal. *Chem. Geol.* **77,** 77–90 (2006).
39. Grossman, E. L. *et al*. Glaciation, aridification, and carbon sequestration in the Permo-Carboniferous: the isotopic record from low latitudes. *Palaeogeogr. Palaeoclimatol. Palaeoecol.* **268,** 222–233 (2008).
40. Romanek, C. S., Grossman, E. L. & Morse, J. W. Carbon isotopic fractionation in synthetic aragonite and calcite: effects of temperature and precipitation rate. *Geochim. Cosmochim. Acta* **56,** 419–430 (1992).
41. Montañez, I. P. Modern soil system constraints on reconstructing deep-time atmospheric CO_2. *Geochim. Cosmochim. Acta* **101,** 57–75 (2013).
42. Woodward, F. I. Plant-responses to past concentrations of CO_2. *Vegetation* **104,** 145–155 (1993).
43. Kurschner, W. M., van der Burgh, J., Visscher, H. & Dilcher, D. L. Oak leaves as biosensors of late Neogene and early Pleistocene paleoatmospheric CO_2 concentrations. *Mar. Micropaleontol.* **27,** 299–312 (1996).

44. Barclay, R. S., McElwain, J. C. & Sageman, B. B. Carbon sequestration activated by a volcanic CO_2 pulse during oceanic anoxic event 2. *Nat. Geosci.* **3,** 205–208 (2010).
45. Steinthorsdottir, M., Jeram, A. J. & McElwain, J. C. Extremely elevated CO_2 concentrations at the Triassic/Jurassic boundary. *Palaeogeogr. Palaeoclimatol. Palaeoecol.* **308,** 418–432 (2011).
46. McElwain, J. C., Beerling, D. J. & Woodward, F. I. Fossil plants and global warming at the Triassic-Jurassic boundary. *Science* **28,** 1386–1390 (1999).
47. Atchison, J. M., Head, L. M. & McCarthy, L. P. Stomatal parameters and atmospheric change since 7500 years before present: evidence from Eremophila deserti (Myoporaceae) leaves from the Flinders Ranges region, South Australia. *Aust. J. Bot.* **48,** 223–232 (2000).
48. Beerling, D. J., Fox, A. & Anderson, C. W. Quantitative uncertainty analyses of ancient atmospheric CO_2 estimates from fossil leaves. *Am. J. Sci.* **309,** 775–787 (2009).
49. McElwain, J. C. & Chaloner, W. G. The fossil cuticle as skeletal record of environmental change. *Palaios* **11,** 376–388 (1996).
50. Steinthorsdottir, M. *Atmospheric CO_2 and Stomatal Responses at the Triassic-Jurassic Boundary* PhD thesis, Univ. College Dublin (2010).
51. McElwain, J. C., Montañez, I. P., White, J. D., Wilson, J. & Yiotis, H. Was atmospheric CO_2 capped at 1000 ppm over the past 300 million years? *Palaeogeogr. Palaeoclimatol. Palaeoecol.* **441,** 653–658 (2016).
52. Boyce, C. K. & Zwieniecki, M. A. Leaf fossil record suggests limited influence of atmospheric CO_2 on terrestrial productivity prior to angiosperm evolution. *Proc. Natl Acad. Sci. USA* **109,** 10403–10408 (2012).
53. Brodribb, T. J., Feild, T. S. & Jordan, G. J. Leaf maximum photosynthetic rate and venation are linked by hydraulics. *Plant Physiol.* **144,** 1890–1898 (2007).
54. White, M. A., Thornton, P. E., Running, S. W. & Nemani, R. R. Parameterization and sensitivity analysis of the BIOME–BGC terrestrial ecosystem model: net primary production controls. *Earth Interact.* **4,** 1–85 (2000).
55. Wilson, J. P. *et al*. Earth-life transitions: paleobiology in the context of Earth system evolution. *Paleontological Society Paper 21* 167–195 (Yale Press, 2015).
56. Dow, G. J., Bergmann, D. C. & Berry, J. A. An integrated model of stomatal development and leaf physiology. *New Phytol.* **201,** 1218–1226 (2014).
57. Pollard, D. & Thompson, S.L. Use of a land-surface-transfer scheme (Lsx) in a global climate model—the response to doubling stomatal-resistance. *Global Planet Change* **10,** 129–161 (1995).
58. Thompson, S.L. & Pollard, D. A global climate model (genesis) with a land-surface transfer scheme (Lsx).1. Present climate simulation. *J. Clim.* **8,** 732–761 (1995).
59. Thompson, S.L. & Pollard, D. Greenland and Antarctic mass balances for present and doubled atmospheric CO_2 from the GENESIS version-2 global climate model. *J. Clim.* **10,** 871–900 (1997).

nature geoscience

SUPPLEMENTARY INFORMATION

DOI: 10.1038/NGEO2822

Climate, p_{CO_2} and terrestrial carbon cycle linkages during late Palaeozoic glacial–interglacial cycles

Authors: Isabel P. Montañez, Jennifer C. McElwain, Christopher J. Poulsen, Joseph D. White, William A. DiMichele, Jonathan P. Wilson, Galen Griggs, Michael T. Hren

AGE MODEL

The stratigraphic distribution of all samples and the age model for relevant successions in all three basins are presented in Supplementary Table 1. The geographic location of Illinois Basin samples are linked to Supplementary Figure 1, whereas outcrop locations and stratigraphic position for samples from the Appalachian and Donets basins are presented in Montañez and Cecil[57] and Eros et al.[18], respectively. The age model provides a chronostratigraphic framework in which to assign absolute ages to the pedogenic carbonates, fossil plants, and coals used in this study. The age model was developed using several sources of information. First, Middle to Late Pennsylvanian cyclothems in the Illinois Basin have been correlated to the time-equivalent succession in the Midcontinent through several decades of field and core studies[10,58]. An *intra*-cyclothem-scale correlation between the Illinois Basin and the Midcontinent, which builds on ref. *58*, is currently in preparation (W. J. Nelson and S. D. Elrick, personal comm., March 2016) as a *Stratigraphic Handbook of Illinois* that will be made publically available online by fall 2016.

Second, Midcontinent 'major' cyclothems[11], which have been hypothesized to be long-eccentricity cycles (405 kyr), have been biostratigraphically correlated to the U-Pb calibrated basin-wide 'marker' limestones within cyclothems (100 kyr durations[18]) of the

Donets Basin[59-60]. Detailed conodont biostratigraphic correlation is possible given that taxonomic turnover occurs at the cyclothem-scale[59]. This cross-Pangean correlation has confirmed the long-eccentricity duration of Midcontinent 'major' cyclothems. Smaller-scale cyclic stratigraphic packages occur within the major cyclothems of the Midcontinent and the Illinois Basin and have been interpreted as short-eccentricity (100 kyr) cycles. Inferred precessional (17 kyr for the Carboniferous[61]) cycles may be nested within the eccentricity-scale cycles[11].

Third, the temporal equivalence of several major cyclothems in the Midcontinent and Illinois Basin to Appalachian Basin cyclothems has been proposed[11,19], tested and shown to be robust[62-63]. For the subset of Appalachian Basin samples used in this study (Supplementary Table 1) these previously defined correlations of major stratigraphic markers to the Midcontinent and Illinois Basin were used.

Fourth, 7 high-precision ID-TIMS U-Pb ages on zircons from tonsteins within the Donets Basin cyclothems[18,64] and the proposed boundary ages of the Geologic Time Scale 2012 (ref. *65*) were used as tie-points to pin the chronostratigraphic framework.

A long-duration eccentricity time-scale was assumed for U.S. '*major*' cyclothems, which coupled with the absolute age tie-points, was used to assign ages to the regionally-developed coals, marine limestones and shales, and intervals of incised channel-filling sandstones within major cyclothems of the Midcontinent and Illinois and Appalachian basins. Inconsistent spacing between cyclothem boundaries shown on Figures 1 and 2, however, reflects the uncertainty in absolute age assignment for the US cyclothems. This is due to the complexity of superimposed scales of cyclicity and the uncertainty of correlation between North American stages and Russian stages of the global time-scale[65].

A thorough discussion of sources of age uncertainty for Carboniferous cyclothems and their global correlation is presented in ref. *66*. The offset by one major cyclothem between the timing of the Late Pennsylvanian peak transgression in the Donets Basin (O7 limestone) and that of the most extensive transgression in the Midcontinent (Oread cyclothem correlated to the O6 Donets limestone, Fig. 2) may reflect the degree of age uncertainty in global correlations. The CO_2 time-series cannot be evaluated for Milankovitch periodicity (i.e., astrochronology) given the inconsistent temporal distribution of carbonate-bearing paleosols and cuticle-containing deposits.

CO_2 MODELING

Sample selection, analytical methodology, and the empirical and modeling approaches for estimating pCO_2 are presented in the Methods section of the online version of the paper. Input data for the pedogenic carbonate-based PBUQ modeling and pCO_2 estimates are presented in Supplementary Table 2 and Supplementary Fig. 4. Input data and pCO_2 estimates for the fossil plant-based SI method and the mechanistic stomatal model are presented in Supplementary Fig. 2 and Supplementary Tables 3 and 4.

BIOME—BGC V. 4.2 TERRESTRIAL ECOSYSTEM MODELING

We simulated ecosystem process for six taxonomic groups representing species that dominated the ecosystems during the period of study using BIOME—BGC v.4.2 (ref. *54*). Vegetation differences were characterized by changing four input parameters: (1) leaf nitrogen, (2) maximum stomatal conductance (G_{max}), (3) boundary layer conductance

(G_b), and (4) specific leaf area (SLA) inferred from the leaf. These groups included two medullosan groups, one representing the species *Macroneuropteris scheuchzeri* and the other non-macroneuropterid Medullosales. The other plant simulation groups represent taxa of *Sphenophyllum*, Lepidodendrales, Cordaitales, and ferns (mostly marattialean tree ferns).

Values of G_{max}, estimated from stomatal trait measurements, were averaged for representative species for each group (Supplementary Table 5) following the protocol of ref. *51*. Leaf boundary layer conductance values (G_b; mol H_2O m^{-2} s^{-1}) were specified for each group to account for leaf size effects on gas exchange. This conductance was calculated based on assuming forced convection transfer where:

$$G_b=0.147du$$

where d is considered to be 0.72 times the mean width of the leaf for simple leaves, or leaflet for complex leaves, or pinnule for fern fronds, and u is the wind speed for which we used a value of 2.0 m s^{-1}. Leaf sizes (and width) for each taxonomic simulation group were approximated from measurements of our samples and published images of fossil leaves for species from each group (Supplementary Table 6).

SLA values for each group (Supplementary Table 7) were derived for taxonomic groups based on their C:N values (Supplementary Tables 6 and 7). The logic for this assumption is based on the leaf economy principle whereby SLA directly modifies change in leaf assimilation with flux rates dependent on leaf nitrogen per unit mass[67]. Linear-regression models (Supplementary Fig. 3) were developed from data for modern New Zealand podocarps (*Phyllocladus trichomanoides*, *Lagarostrobus colensoi*, *Dacrydium cupressinum*, *Podocarpus totara*, *P. cunninghamii*, *Prumnopitys ferrugiea*) and tree ferns

(*Cyathea smithii* and *Dickonsonia squarrosa*)[68]. Medullosales, Lepidodendrales, and Cordaitales SLA values were derived from the regression model for podocarps using median carbon to nitrogen ratios (C:N) for these species. The C:N ratios for these groups are from Montañez and Griggs, unpublished data. Extinct tree fern SLA were predicted from the New Zealand fern models. For *Sphenophyllum*, we used the mean SLA reported for modern *Equisetum* sp. (ref. *69*). Final parameters for each representative taxonomic group input to BIOME—BGC v.4.2 are presented in Supplementary Table 7.

For paleo-atmospheric pCO_2 inputs into the model, we used median values for specific intervals derived by this study. The values were selected to represent a physiologically active range of pCO_2 from extreme low to high. Atmospheric pO_2 was estimated for each time period[5,70-71] and the associated changes in atmospheric pressure (P), molecular weight of air (M_a) and specific heat of air with constant pressure (c_p) were calculated to account for variation in major drivers of evaporation. Values of atmospheric pressure (P) and the molecular mass of air (M_a) were derived from pO_2 based on ref. *9*. The values of specific heat of air with constant pressure (c_p) were calculated from Ma values $c_p = (7/2)(R/M_a)$, where R is the ideal gas constant. Atmospheric input properties for the BIOME-BGC v.4.2 simulations run during this study are presented in Supplementary Table 8. Daily meteorological data input into the BIOME-BGC v.4.2 model are from the National Centers for Environmental Prediction (NCEP) Climate Forecast System Reanalysis (CFSR) for the period of 1979 through 2014. From this global dataset, we chose the data for N 2.2681° and W-77.4976°, located near the Rio Macuma, Ecuador, as a tropical rainforest climate. Mean annual temperature for this location is currently 20.5°C with

annual precipitation of 730 cm/year. For our simulations, we increased daily temperature values by 5°C to represent the mean paleoclimate for the analysis.

For each time period, simulations for each group were run for 36 years (the length of the meteorological data) using the time appropriate atmospheric characteristics. From these simulations, mean daily net canopy assimilation values (A; μmol CO^2 m^{-2} s^{-1}) and transpiration values (E; mmol H_2O m^{-2} s^{-1}) were collected and assessed to calculate water use efficiency (A/E) or WUE (Fig. 3).

STATISTICAL ANALYSIS OF CO_2 RESULTS & PHYSIOLOGICAL CO_2 THRESHOLD

The default output for PBUQ is a best estimate of pCO_2 presented as median values of the Monte Carlo population and 16^{th} and 84^{th} percentile uncertainties. Probability density functions of calculated $[CO_2]_{atm}$ are slightly skewed toward high values, in large part due to the Soil Order-based skewed S(z) distributions, in particular for Vertisols. In this study, reported best estimates of CO_2 are presented as interquartile mean values (i.e., 25% trimmed/truncated mean) rather than median values given that the truncated mean removes the influence of very high and low CO_2 estimates defined by outliers in the skewed S(z) input dataset. The 16^{th} and 84^{th} percentile uncertainties, however, are based on the untrimmed distribution of Monte Carlo CO_2 estimates so as to capture the full range of modeled values.

A truncated mean is a robust estimator of centrality for mixed distributions and skewed data sets as it is less sensitive to outliers, such as those created by the few but high S(z) values for Vertisols, than the statistical mean, but still provides a reasonable estimate of

136 central tendency for a population of data. A comparison of the median and interquartile
137 mean values of best estimates of CO_2 (Supplementary Fig. 4) indicates minimal
138 difference between estimated CO_2 values for Protosols and Argillisols (a few ppm) and a
139 slight difference between values for Calcisols (40 ppm ±17 ppm). For Vertisols, an
140 average difference of 122 ppmv (±28 ppm) occurs between modeled median and
141 interquartile mean values.

142 We consider the interquartile mean values as the more robust estimates of $[CO_2]_{atm}$ given
143 that 27% of the modeled *median* best estimates of CO_2 are biologically untenable
144 (negative to <150 ppm). This reflects that CO_2 estimates <150 ppm are close to the
145 modeled (BIOME—BGC v.4.2) physiological limit for efficient carbon assimilation
146 relative to transpiration water loss and thus the lower limit for sustained primary plant
147 production over the hypothesized atmospheric O_2 range for the Pennsylvanian and early
148 Permian (21 to 35% (refs. *5*, *70*, *71*)). Below ~150 ppm, late Paleozoic medullosans
149 could not sufficiently assimilate CO_2 due to critical limits of internal CO_2 concentrations
150 within the leaf tissue that are too low to sustain cellular respiratory demands of the leaf
151 tissue with increased photorespiratory effects on reduced quantum efficiency of
152 photosynthesis. Therefore, at CO_2 concentrations below this threshold, it is likely that late
153 Carboniferous and early Permian plants were incapable of growing to fully capture water
154 and nutrient resources of their habitat and that only limited vegetation coverage could
155 have been sustained over the late Paleozoic landscape[27,28,72].

156 To further assess the influence of low atmospheric pCO_2 on plant function, we fit, for
157 each species, the WUE values for each CO_2 estimate derived from the ecosystem
158 modeling (BIOME—BGC v4.2) with a Michaelis-Menten function (Supplementary Fig.

159 5). From these BIOME-BGC simulations, values of maximum velocity (i.e. maximum
160 WUE; v_{max}) and the half-saturation value of atmospheric CO_2 (K_m) were estimated from
161 the data using a Lineweaver-Burk transformation. We subsequently estimated a linear
162 function using the value of 0.5 (v_{max}) representing a 50% reduction in WUE at a CO_2
163 level (K_m) assuming that WUE is 0.0 at approximately 90 ppm for each species. We
164 found that WUE was, on average, 50% of maximum at 250 ppm and 18% at 150 ppm.
165 This analysis supports our conclusion that atmospheric CO_2 levels ≤150 ppm would
166 severely reduce plant productivity. In addition, our simulations were for a wet tropical
167 location and thus not water-limited. In water-limited environments, this constraint would
168 make the majority of vascular-plant life non-sustainable.

169 Furthermore, for those periods of low atmospheric CO_2 (and high O_2) concentrations (i.e.,
170 the deep glacials of the MLPB and earliest Permian) the gas-exchange capacity and
171 photosynthetic physiology of late Paleozoic plants likely varied in their sensitivity to
172 these atmospheric conditions. Taxa with a high total conductance to CO_2 (i.e., high
173 stomatal conductance (G_{max}) and/or high mesophyll conductance ($G_{m(max)}$) would have
174 had an ecophysiological advantage under low CO_2 relative to taxa of lower conductance
175 given the need to maximize CO_2 concentration at the site of carboxylation and minimize
176 photorespiration within plant tissues[27,28]. The anatomical manifestation of high stomatal
177 conductance in the fossil record include fossil taxa with high stomatal density and/or
178 stomatal pore size, moderate to high vein densities, and an absence of stomatal crypts.
179 The anatomical manifestation of high mesophyll conductance in the fossil record are low
180 leaf tissue density, high mesophyll tissue aeration via air spaces, and low mesophyll cell
181 wall thickness[73-74]. For the late Paleozoic, vein density and estimated G_{max} were

substantially higher for Medullosales (2 to 5 mm mm^{-2} and up to 3 mole m^{-2} s^{-1}, respectively, (ref. *55*) and tree ferns (1.5 to 3.5 mm mm^{-2} (ref. *75*)) than for Lepidodendrales (single vein, few stomata, and G_{max} of 0.2 to 0.8 mole m^{-2} s^{-1} (ref. *76*)).

LOESS Analysis of pCO_2 estimates: The consensus CO_2 curve determined using paleosol, stomatal ratio, and mechanistically based stomatal estimates of pCO_2 (Fig. 2) was defined using a locally weighted polynomial regression (LOESS) available from PAST freeware[77]. This nonparametric regression places higher significance on individual data points, which are clustered more than on those that plot further apart or are outliers. A 0.1 smoothing was chosen in order to minimize introducing bias into the estimation process and in order to capture the full degree of temporal variability in the pCO_2 estimates. Comparison of the LOESS results for the pedogenic carbonate-based CO_2 estimates using a 0.1, 0.3, or 0.5 smoothing parameter (Supplementary Fig. 6) indicates that the long-term trend in CO_2 is captured in all three smoothing analyses including million year-scale variability (e.g., minimum at ~306 to 305 Mya and maximum at ~303 Mya).

In order to further objectively evaluate the robustness of a 0.1 smoothing we used a cross-validation approach in which a series of LOESS runs were carried out after excluding 10% of the data points from the algorithm. Data points were excluded from five different subsets of the full dataset by excluding every 10^{th} point beginning with the 2^{nd}, 4^{th}, 6^{th}, 8^{th}, and 10^{th} data point. Supplementary Figure 7 illustrates the complete overlap of the five LOESS analyses indicating that each estimate predicted well the excluded data points and confirming that a 0.1 smoothing parameter for the LOESS algorithm and the high-resolution consensus CO_2 record we report here is robust.

205

206 **CONSTRAINING TERRESTRIAL CARBON SEQUESTRATION & POTENTIAL OTHER C**

207 **SOURCES/SINKS**

208 Our pCO_2 reconstruction for the latter half of the Pennsylvanian and earliest Permian
209 indicates 200 to 300 ppm-scale changes at the 10^5-yr scale that translate to a magnitude
210 of increase in the atmosphere of 425 to 650 GtC, and up to 1000 GtC during the early
211 Gzhelian peak in CO_2. Given ~50% sequestration by other C sinks, the total amount of
212 carbon released to the atmosphere within each 10^5-year cycle may have been double
213 these estimates (850 to 2000 GtC). For comparison, we calculated the carbon
214 sequestration potential of lycopsid-dominated coal forests, which populated the tropical
215 lowlands during Early and Middle Pennsylvanian glacials[21], and the consequent change
216 in CO_2 influx to the atmosphere in response to climate-driven 10^5-yr scale reorganization
217 of vegetation during deglaciations and interglacials. The following discussion addresses
218 the *potential* of the tropical wetland forest biome as well as high-latitude tundra to
219 sequester carbon during different climate phases and CO_2 concentrations. We were not,
220 however, able to quantify, through modeling, the global net source or sink of C at any
221 given point in time.

222 ***Geological Model***: We provide the following geological model as a context for potential
223 changes in carbon sequestration by tropical wetland forests and high-latitude tundra
224 throughout one eccentricity-scale glacial-interglacial cycle and over the range of 280 to
225 840 ppm CO_2. Lithofacies within cyclothems have long been mechanistically linked to
226 glacieustatic and climate changes through an eccentricity-scale glacial-interglacial cycle
227 (e.g. refs *2, 11, 18, 63*, *78* and citations within). Cycles are bounded by erosional
228 surfaces, some with sandstone-filled deeply incised channels (a few meters to 30+ m),

229 which record the forced regression of sea level during renewed ice buildup (early glacial)
230 as eccentricity modulation shifted from high to low and obliquity was rising (Phase I (160
231 to 175 kyr) on Supplementary Fig. 8). Maximum accumulation of ice (lowstand), during
232 low eccentricity modulation (and low obliquity), is recorded in cyclothems by widespread
233 development of paleosols and continued landscape erosion (Phase II on Supplementary
234 Fig. 9); incised-valley fills (major IVFs on Fig. 2) were deposited throughout ice buildup
235 and the early lowstand. Overlying coals were deposited during the late glacial as the rate
236 of sea level fall slowed and was outpaced by the regional subsidence rates providing
237 accommodation for peat and sediment accumulation (Phase III on Supplementary Fig. 8).
238 Peat accumulation predated the onset of sea-level rise (225 to 235 kyr on Supplementary
239 Fig. 8) driven by rapid ice sheet ablation with the return to a high eccentricity phase[18,78].
240 This argument for peat accumulation predating sea-level rise reflects that (1) there is no
241 modern or geologic evidence that rising sea level paludifies coastal regions and creates an
242 inwardly migrating band of peat; (2) peats, which sourced Pennsylvanian coals, are of a
243 thickness and low ash content that in modern analogues are entirely a product of
244 rainfall/climatic conditions and not an expression of rising-sea-level; (3) many North
245 American coals are overlain by a ravinement (erosional) surface that marks the onset of
246 transgression; (4) climate simulations[78] indicate that the deglaciation would have been
247 more highly seasonal than any other period of the glacial-interglacial cycle. The ensuing
248 rapid sea-level rise of deglaciation is recorded by siliciclastics including thick wedges of
249 siltstone tidalites lining channels contemporaneous with peat but truncated by the
250 ravinement surface and by overlying black marine shales (Phase IV on Supplementary
251 Fig. 8). Carbonates and deltaic siliciclastics were deposited as eustatic rise rates slowed

toward the sea-level highstand and accommodation space decreased (235—240 kyr on Supplementary Fig. 8)[18,78].

There is disparity in the inferred polarity of climate changes during glacials and interglacials with some empirical models suggesting drier and less seasonal glacials than interglacials and others arguing for everwet glacials and drier, more seasonal interglacials (summarized in ref. *2*). Notably, our late Paleozoic climate simulations indicate that shifts in mean annual precipitation (MAP) and intensity of seasonality occurred *within* the glacial and interglacial periods given the influence of eccentricity modulation of precessional forcing of climate in the paleotropics[6,78]. Interglacials and early glacials (Phases IV and I on Supplementary Fig. 9) were characterized by highly variable and strongly seasonal climate including alternation between precessional-scale drier and wetter periods (Supplementary Fig. 8). In contrast peak (Phase II) and late glacials (Phase III) were generally wetter and characterized by far less variable distribution of seasonal precipitation governed by low eccentricity modulation. Overall more annually equable rainfall distibution, with rainfall exceeding evapotranspiration for most of the year, during the late glacials would have elevated the water table and stabilized soil surfaces with vegetation, thus permitting the widespread expansion of coal forests and accumulation of peats (Phase III on Supplementary Fig. 8).

C Sequestration Potential of Tropical Wetland Forests During Maximum Expansion: As a first step in evaluating the carbon sequestration potential of tropical wetland forests, we estimated carbon sequestration rates, using a carbon biomass for lycopsids (3200 kg C/plant) and a tree density per hectare of 500 to 1800 (ref. *8*); lycopsids make up the majority of preserved organic matter in many Carboniferous coals. Assuming a century-

scale lifespan[76] and a proposed maximum areal extent of 2400 X 10^3 km^2 for these tropical forests (late Moscovian time)[8], then the global potential to sequester carbon by lycopsid-dominated forests was between 3.9 and 13.9 gigatons of carbon per year (GtC/yr). This range is an order of magnitude less than suggested by Cleal and Thomas[8] reflecting their use of a decadal-scale lycopsid lifespan. Estimates of potential carbon sequestration are *minimum* values given that (1) they do not account for accumulation of organic matter from other flora such as Medullosales (~20 to 30% of biomass) and marattialean tree ferns (~10%) and (2) the maximum areal extent of 2400 X 10^3 km^2 is an order of magnitude smaller than indicated by late Paleozoic climate simulations[6,79] for the 'wetland forest' extent over a range of pCO_2 (280 to 840 ppm). Preservation of vegetation litter in the wetland environments was higher than in modern tropical forests given the low pH substrates and high long-term accumulation rates of peat as coal[66]. We assume 25% of the C is recycled to the atmosphere through heterotrophic respiration and another ~5% is lost through surface runoff and CO_2 fertilization (cf. ref. *8*). On the basis of these assumptions, the potential of the lycopsid-dominated forests, which prospered during glacial periods, to sequester C is estimated to be ~3 to 10 GtC/yr (or 1.4 to 4.7 ppm CO_2/yr). Although this estimate does not account for temporal changes in the areal extent of the wetland forests, it demonstrates a C sequestration potential of wetland forests far greater than needed to account for the 200 to 300 ppm drop in CO_2 during glacial periods.

Dynamic Changes in Terrestrial Carbon Sequestration: In order to evaluate the influence on carbon sequestration potential of *dynamic* changes in paleotropical vegetation and extent of high-latitude tundra in response to changing climate and CO_2,

298 we evaluated modeled changes in areal extent of dominant paleo-tropical biomes
299 (wetland forests vs. combined tropical xerophytic shrubland, desert, and barren land)
300 throughout an eccentricity cycle over a range of relevant CO_2 concentrations (280 to 840
301 ppm) (Supplementary Table 9). Late Paleozoic climate simulations[6] indicate a decrease
302 of as much as 6.7% (under CO_2 concentrations of 420 ppm) in the areal extent of the
303 wetland forests from the glacial to interglacial periods and replacement by lower biomass
304 and lower carbon density shrubland and desert/barren land in response to orbitally forced
305 changes in solar insolation throughout an eccentricity cycle. Maximum extent of the
306 wetland forest biome occurs throughout ice growth and typically peaks during maximum
307 ice accumulation for a prescribed CO_2 concentration ('peak glacial' and 'late glacial' in
308 Supplementary Table 9). A much larger decrease (26.4%; decreasing from 50.1 to 23.7%)
309 in areal extent of wetland forests, estimated using maximum percentage of wetland
310 forests for each CO_2 simulation, occurs in response to increasing CO_2 from 280 to 840
311 ppm, a finding in line with previous climate simulations of vegetation sensitivity to late
312 Paleozoic ice volume and atmospheric pCO_2 (ref. *79*) and paleobotanical data[8]. Given
313 that both insolation intensity and pCO_2 varied through an orbital cycle, we used a
314 conservative range (6 to 10%) of vegetation redistribution to calculate the change in C
315 sequestration potential with increasing solar insolation and CO_2. This range translates to a
316 decrease in the tropical vegetation carbon sink from peak/late glacial periods to
317 interglacial times of ~0.2 to 1 GtC/yr. In turn, this would lead during deglaciation to an
318 increase in CO_2 flux to the atmosphere of 0.1 to 0.5 ppm/year (2.13 GtC per ppm change
319 in CO_2), an estimate that is two orders of magnitude higher than inferred from our
320 Pennsylavanian pCO_2 record. Repeated drought episodes as the climate warmed during

321 the deglaciation could have further reduced the paleotropical C sink and increased the
322 estimated CO_2 efflux from tropical vegetation, a process that would have been
323 accelerated by intermittent seasonal or precessional-scale wetting (cf. ref. *80*).

324 Scaling the aforementioned assumptions up to the proposed 25 to 50% contraction of
325 the tropical wetland forests[8] on a 10^6-yr scale through the late Pennsylvanian and early
326 Permian yields a decrease in this biome's C sequestration potential of 0.8 to 5 GtC/yr or
327 an increase in CO_2 flux to the atmosphere of up to 0.4 to 2.4 ppm/year, again more than
328 sufficient to accommodate the longer-term increase in CO_2 concentration *circa* 304 to
329 303 Mya. The actual increase in atmospheric CO_2 in response to a reduced terrestrial C
330 sink, however, would have been smaller (perhaps by up to 50%) due to absorption of CO_2
331 by surface C sinks (e.g., the ocean, other biomes).

332 Climate simulations for the late Paleozoic ice age[6] further indicate that the areal
333 extent of tundra could have varied by up to 15.7% (at 560 ppm) within an orbital cycle
334 due to changes in high-latitude solar insolation (Supplementary Table 9). For example,
335 simulated tundra (for CO_2 of 560 ppm) expands to 18% of global surface area in response
336 to the solar insolation minimum during the *late* interglacial period (160 kyr on
337 Supplementary Fig. 8) from an average of 3.7% throughout ice accumulation (early
338 through late glacial). This 10^4-yr increase in tundra, which is coincident with the solar
339 insolation minimum that initiates renewed ice buildup, translates to an increase in areal
340 extent of 17,845 X 10^3 km^2. Applying a permafrost soil C density of 30 to 60 kg C m^{-2},
341 which includes coldest mineral soils[81], to this increase in tundra scales up to an increase
342 in C sequestration potential of 535 to 1070 GtC. Importantly, this increased short-lived C
343 sink suggests a potential rapid decrease in CO_2 flux to the atmosphere during the turnover

344 to glacial conditions of up to 250 to 500 ppm. The net change in global terrestrial C
345 storage, however, would depend on the sequestration potential of all biomes at that time.
346 In contrast, the much slower release rate of the C sequestered in tundra to the atmosphere
347 (0.0025 to 0.01 ppm CO_2/yr) during the longer-term (10^5-yr) buildup of ice sheets, when
348 tropical wetland forests expanded, is 1 to 2 orders of magnitude slower than the potential
349 C sequestration rate of wetland forests (0.4 to 2.4 ppm/yr).

350 ***Additional Controls on late Paleozoic C Cycling***: The role of the oceans in late Paleozoic
351 C cycle dynamics is poorly constrained given limited constraints on paleo-ocean
352 productivity, paleo-ocean structure and circulation, and phytoplankton compositions
353 during the period of interest. Moreover, the deep-sea carbonate buffering feedback that
354 has regulated pCO_2 since the Cretaceous and factored prominently in governing
355 Pleistocene CO_2 fluctuations did not exist in the Carboniferous (Neritan) ocean given that
356 carbonate-shelled primary producers had not yet evolved. Eccentricity paced changes in
357 the ocean carbon reservoir, through modulation of precessional-forcing of low-latitude
358 climate, however, could have further contributed to the interglacial rises of Carboniferous
359 short-term CO_2 fluctuations (cf. ref. *82-83*). This C source may have been amplified due
360 to the climate system's enhanced sensitivity to eccentricity-paced changes in the C
361 reservoirs of Neritan oceans. Lastly, magmatic CO_2 may have further contributed to
362 short-term CO_2 fluctuations in the Pennsylvanian and early Permian through variation in
363 subareal and ocean-ridge volcanism on a 10^5-kyr scale governed by feedbacks between
364 ice sheet unloading/loading, eustatic change, and mantle decompression[84-85].

365 On the million-yr scale, the progressive restructuring and demise of the tropical coal-
366 swamp forests due to intensified aridification through the Late Pennsylvanian and early

Permian would have reduced the sequestration potential of the tropical terrestrial biome. Major contraction of wetland forests (25 to 50% (ref. *8*)) may have contributed to the late Pennsylvanian (304 to 303 Mya) increase in pCO_2 (Fig. 2) given the potential CO_2 flux to the atmosphere of several ppm/yr (see previous discussion). The decoupling of the very low pCO_2 of the deep glacials (i.e., early Permian) from the anticipated long-term decrease in terrestrial C sequestration, however, necessitates the influence of additional longer-term C sinks. Increased silicate weathering associated with uplift of the Central Pangaean Mountains during Pennsylvanian—early Permian continental reorganization undoubtedly influenced the long-term evolution of pCO_2. Quantifying the contribution of this sink, however, awaits improved chronologic constraints on the timing of discrete tectonic events[86]. In addition, permafrost may have provided an additional major C sink if tundra expanded greatly during the long-term deep glacials.

SUPPLEMENTARY REFERENCES

57. Montañez, I. P. & Cecil, C. B. Paleoenvironmental Clues Archived in Non-Marine Pennsylvanian-lower Permian Limestones of the Central Appalachian Basin, USA. *Int. J. Coal Geology* **119**, 41-55 (2013).

58. Nelson, W. J., Khorasgani, Z. A. & Elrick, S. D. Revised Upper Pennsylvanian stratigraphy of Illinois Basin with regional correlations. *Geol. Soc. Amer. Abst. Prog.* **43**, 249-18 (2011).

59. Heckel P. H. *et al*. Cyclothem [‘‘digital’’] correlation and biostratigraphy across the global Moscovian-Kasimovian-Gzhelian stage boundary interval (Middle-Upper Pennsylvanian) in North America and eastern Europe. *Geology* **35**, 607–610 (2007).

60. Schmitz, M. D. & Davydov, V. I. Quantitative radiometric and biostratigraphic calibration of the Pennsylvanian–Early Permian (Cisuralian) time scale and pan-Euramerican chronostratigraphic correlation. *Geol. Soc. Am. Bull.* **124**, 549–577 (2012).

61. Berger, A. & Loutre, M. F. in *Orbital Forcing and Cyclic Sequences*, P. L. De Boer and D. G. Smith Eds. (Blackwell, London, 1994), Internat. Assoc. Sediment. Spec. Publ. 19, pp.15-24.

62. Falcon-Lang, H. J. *et al*. No major stratigraphic gap exists near the Middle-Upper Pennsylvanian (Desmoinesian-Missourian) boundary in North America. *Palaios* **26**, 125-139 (2011).

63. Cecil, B., DiMichele, W. A. & Elrick, S. D. Middle and Late Pennsylvanian cyclothems, American Midcontinent: Ice-age environmental changes and terrestrial biotic dynamics. *Comptes Rendus Geosci.* **346**, 159-168 (2014).

64. Davydov, V. I., Crowley, J. L., Schmitz, M. D. & Poletaev, V. I. High-precision U–Pb zircon age calibration of the global Carboniferous time scale and Milankovitch-band cyclicity in the Donets Basin, eastern Ukraine. *Geochem. Geophys. Geosyst.* **11**,1–22 (2010).

65. Davydov, V. I., Korn, D. & Schmitz, M. D. in *The Geologic Time Scale 2012*, Gradstein, F., Ogg, J., Schmitz, M. and Ogg, G., Eds. (Elsevier, London, 2012), vol. 1, pp. 615-663.

66. van den Belt, F. J. G., van Hoof, T. B. & Pagnier, H. J. M. Revealing the hidden Milankovitch record from Pennsylvanian cyclothem successions and implications regarding late Paleozoic chronology and terrestrial-carbon (coal) storage. *Geosphere* **11** (2015). Doi:10.1130/GESO1177.1

67. Poorter, H., H. Lambers & J.R. Evans. 2014. Trait correlation networks: a whole-plant perspective on the recently criticized leaf economic spectrum. New Phytologist 201: 378–382.

68. White, J.D. & Scott, N.A. 2006. Specific leaf area and nitrogen distribution in New Zealand forests: species independently respond to intercepted light. Forest Ecology and Management. 226:319-329.

69. van Wijk, M.T., Williams, M. & Shaver, G.R. 2005. Tight coupling between leaf area index and foliage N content in arctic plant communities. Oecologia 142: 421–427.

70. Bergman, N. M., Lenton, T. M. & Watson, A. J. COPSE: A new model of biogeochemical cycling over Phanerozoic time. *Am. J. Sci.* **304**, 397-437 (2004).

71. Glasspool, I. J. & Scott, A. C. Phanerozoic concentrations of atmospheric oxygen reconstructed from sedimentary charcoal. *Nat. Geosci.* (2010). DOI:10.1038/NGEO923

428 72. Prentice, I.C. & Harrison, S.P. Ecosystem effects of CO_2 concentration: evidence
429 from past climates. *Clim. Past* **297**, 297-307 (2009).

430 73. Tomás, M. *et al*. Importance of leaf anatomy in determining mesophyll diffusion
431 conductance to CO_2 across species: quantitative limitations and scaling up by models.
432 *J. Exper. Botany* **64**, 2269-2281 (2013).

433 74. Tosens, T. *et al*. Anatomical basis of variation in mesophyll resistance in eastern
434 Australian sclerophylls: news of a long and winding path. *J. Exper. Botany* **63**, 5105-
435 5119 (2012).

436 75. Boyce, C. K., Brodribb, T., Feild, T. S. & Zwieniecki, M. A. Angiosperm leaf vein
437 evolution was physiologically and environmentally transformative. *Proc. Royal Soc.*
438 *London B* **276**, 1771-1776 (2009).

439 76. Boyce, C. K. & W. A. DiMichele, W. A. Arborescent lycopsid productivity and
440 lifespan: Constraining the possibilities. *Rev. Palaeobot. Palynol.* **227**, 97-110 (2016).

441 77. Hammer, Ø., Harper, D.A.T. & Ryan, P. D. PAST: Paleontological statistics
442 software package for education and data analysis. Palaeontologia Electronica **4**
443 (2001). http://palaeoelectronica.org/2001_1/past/issue1_01.htm

444 78. Horton, D.E., Poulsen, C.J., Montañez, I.P. & DiMichele, W.A. Eccentricity-paced
445 late Paleozoic climate change and its role in cyclostratigraphy: *Palaeogeograph.,*
446 *Palaeoclimatol., Palaeoecol.* **331**, 150-161 (2012).

447 79. Poulsen, C.J., Pollard, D., Montañez, I.P. & Rowley, D. Late Paleozoic tropical
448 climate response to Gondwanan deglaciation. *Geology* **35**, 771-774 (2007).

449 80. Fenner, N. & Freeman, C. Drought-induced carbon loss in peatlands. *Nat. Geosci.* **4**,
450 895-900 (2011).

451 81. Ciais, P. *et al*. Large inert carbon pool in the terrestrial biosphere during the Last
452 Glacial Maximum. *Nat. Geosci.* **5**, 74-79 (2011)

453 82. Sexton, P. F. *et al*. Eocene global warming events driven by ventilation of ocean
454 dissolved organic carbon. *Nature* **471**, 349-353 (2011).

455 83. Wang, P., Tian, J. & Lourens, L. J. Obscuring of long eccentricity cyclicity in
456 Pleistocene oceanic carbon isotope records. *Earth Planet. Sci. Lett.* **290**, 319-330
457 (2010).

458 84. Tolstoy, M. Mid-ocean ridge eruptions as a climate valve. *Geophy. Res. Lett.* **42**,
459 1346-1351 (2015).

460 85. Huybers, P. & Langmuir, C. Feedback between deglaciation, volcanism, and
461 atmospheric CO_2. *Earth Planet. Sci. Lett.* **286**, 479-491 (2009).

462 86. Torsvik, T. H. *et al*. Phanerozoic polar wander, palaeogeography and dynamics.
463 *Earth-Sci. Rev.* **114**, 325-368 (2012).

464 87. Bomfleur, B. & Kerp, H. *Dicroidium* diversity in the Upper Triassic of north Victoria
465 Land, East Antarctica. *Rev. Palaeobot. Palynol.* **160**, 67-101 (2010).

466 88. Reihman, M. A. & Schabilion, J. T. Cuticles of two species of Alethopteris. *Amer. J.*
467 *Botany* **63**,1039-1046 (1976).

468 89. Stidd, L. L. O. & Stidd, B. M. Paracytic (syndetocheilic) stomata of Carboniferous
469 seed ferns. *Science* **193**,156-157 (1976).

90. Krings, M. & Kerp, H. Morphology, Growth Habit, and Ecology of *Blanzyopteris praedentata* (Gothan) *nov. comb*., a Climbing Neuropteroid Seed Fern from the Stephanian of Central France. *Internat. J. Plant Sci.* **160**, 603-619 (1999).

91. Cleal, C. J. & Shute, C. H. Epidermal features of some Carboniferous neuropteroidfronds. *Rev. Palaeobot. & Palynol.* **71**, 191-206 (1992).

92. Shute, C. H. & Cleal, C. J. Ecology and growth habit of Laveineopteris: A gymnosperm from the late Carboniferous tropical rain forests. *Palaeontol.* **45**, 943-972 (2002).

93. Krings, M. & Kerp, H. Cuticles of Lescuropteris genuina from the Stephanian (Upper Carboniferous) of Central France: evidence for a climbing growth habit. *Botan. J Linnean Soc.* **123**, 73-89 (1997).

94. Cleal, C. J. & Zodrow, E. I. Epidermal structure of some Megullosan Nureopteris folage from the middle and upper Carboniferous of Canada and German. *Palaeontology* **32**, 837-882 (1989).

95. Zodrow, E. I. & Cleal, C. J. The epidermal structure of the Carboniferous gymnosperm frond Reticulopteris. *Palaeontology* **36**, 65-79 (1993).

96. Stidd, B. M. & Phillips, T. L. The Vegetative Anatomy of Schopfiastrum decussatum from the Middle Pennsylvanian of the Illinois Basin. *Amer. J. Botany* **60**, 463-474 (1973).

97. Psenicka, J. & Bek, J. Cuticles and spores of Senftenbergia plumosa (Artis) Bek and Psenicka from the Carboniferous of Pilsen Basin. *Rev. Palaeobot. & Palynol.* **125**, 299-312 (2003).

492 98. Yao, Z.-Q., Liu, L.-J., Mapes, G. & Rothwell, G.W. Leaf morphology and cuticular
493 features of *Sphenophyllum* in the *Gigantopteris* flora from South China. *Rev.*
494 *Palaeobot. & Palynol.* **110**, 67–92 (2000).

495 99. Batenburg, L. H. Vegetative anatomy and ecology of *Sphenophyllum zwickaviense*, *S.*
496 *emarginatum*, and other "compression species" of *Sphenophyllum*. *Rev. Palaeobot. &*
497 *Palynol.* **32**, 275-313 (1981).

498 100. Hetterscheid, W. L. & Batenburg, L. H. Sphenophyllum miravallis Vetter and
499 Bowmanites cupulatus sp. n. from the "Illinger Flözzone"("Heusweiler Schichten",
500 Lower Stephanian, Saar Basin, German Federal Republic). *Rev. Palaeobot. &*
501 *Palynol.* **40**, 263-293 (1984).

502 101. Pant, D. D. & Mehra, B. On the epidermal structure of *Sphenophyllum speciosum*
503 (Royle) Zeiller. *Palaeontograph. Abteilung B Band* **112**, 51-57 (1963).

504 102. Šimůnek, Z. & Bureš, J. Dispersed cuticles and conducting tissue of *Sphenophyllum*
505 BRONGNIART from the Westphalian D of Kalinovo, Donets Basin, Ukraine.
506 *Geologia Croatica* **68**, 1-9 (2015).

507 103. Thomas, B. A. The cuticle of two species of *Bothrodendron* [Lycopsida:
508 Lepidodendrales]. *J. Nat. Hist.* **1**, 53-60 (1967).

509 104. Thomas, B. A. Epidermal studies in the interpretation of *Lepidodendron* species.
510 *Paleontol.* **13**, 145-173 (1970).

511 105. Thomas, B. A. The cuticle of the Lepidodendroid stem. *New Phytol.* **65**, 296-303
512 (1966).

513 106. Thomas, B. A. Epidermal studies in the interpretation of *Lepidoploios* species.
514 *Paleontol.* **20**, 273-293 (1977).

515 107. Thomas, B. A. The carboniferous fossil lycopod *Ulodendron landsburgii* (Kidston)
516 comb. nov. *J. Nat. Hist.* **2**, 425-428 (1968).

517 108. Šimůnek, Z. & Florjan, S. The Pennsylvanian cordaitalean dispersed cuticles from
518 the Upper Silesian Basin (Poland). *Rev. Palaeobot. & Palynol.* **197**, 26-49 (2013).

519 109. Šimůnek, Z. New classification of the genus *Cordaites* from the Carboniferous and
520 Permian of the Bohemian Massif based on micromorphology of its cuticle. *Acta*
521 *Musei Nationalis Pragae, Series B Historia Naturalis* **62**, 97–210 (2007).

522 110. Šimůnek, Z., Opluštiland, S. & Drábková, J. *Cordaites borassifolius* (Sternberg)
523 Unger (Cordaitales) from the Radnice Basin (Bolsovian, Czech Republic). *Bull.*
524 *Geosci.* **84**, 301–336 (2009).

525 111. Zodrow, E. L., Imunek, Z. & Bashforth, A. R. New cuticular morphotypes of
526 Cordaites principalis from the Canadian Carboniferous Maritimes Basin. *Canad. J.*
527 *Bot.*, 78(2), 135-148 (2000).

528 112. Pšenička, J. Taxonomy of Pennsylvanian-Permian ferns from coal basins in the
529 Czech Republic and Canada. Ph.D. thesis, Faculty of Science, Charles Univ.,
530 Prague, 1–185 (2005).

531 113. Stamps, R. H., Nell, T. A. & Barrett, J. E. Production temperatures influence
532 growth and physiology of leatherleaf fern. *Horticult. Sci.* **29**, 67-70 (1994).

533 114. Durand, L. Z. & Goldstein, G. Photosynthesis, photoinhibition, and nitrogen use
534 efficiency in native and invasive tree ferns in Hawaii. *Oecologia* **126**, 345–354
535 (2001).

536 115. Pšenička, J., Bek, J., Zodrow, E. L., Cleal, C. J. & Hemsley, A. R. A new late
537 Westphalian fossil marattialean fern from Nova Scotia. *Bot. J. Linnean Soc.* **142**,
538 199–212 (2003).

539 116. Stull, G. W., DiMichele, W. A., Falcon-Lang, H. J., Nelson, W. J. & Elrick, S.
540 Palaeoecology of *Macroneuropteris scheuchzeri*, and its implications for resolving
541 the paradox of 'xeromorphic' plants in Pennsylvanian wetlands. *Palaeogeograph.,*
542 *Palaeoclimatol., Palaeoecol.* **331–332**, 162–176 (2012).

543 117. Ramanujam, C. G. K., Rothwell, G. W. & Stewart, W. N. Probable attachment of
544 the *Dolerotheca campanulum* to a *Myeloxylon-Alethopteris* type frond. *Amer. J.*
545 *Botany* **61**, 1057-1066 (1974).

546 118. Krings, M., Klavins, S. D. , DiMichele, W. A., Kerp, H. & Taylor, T.N. Epidermal
547 anatomy of *Glenopteris splendens* Sellards nov. emend., an enigmatic seed plant
548 from the Lower Permian of Kansas (U.S.A.) *Rev. Palaeobot. & Palynol.* **136**, 159 –
549 180 (2005).

550 119. Scott, D. H. On the structure and affinities of fossil plants from the Palaeozoic
551 rocks. III. on *Medullosa anglica*, a new representative of the Cycadofilices.
552 *Proceed. Royal Soc. Lond.* **64**, 249-253 (1898).

120. Krings, M. & Kerp, H. *Neuropteris attenuata*, a narrow-stemmed, leaning or lianescent seed fern from the Upper Pennsylvanian of Lower Saxony, Germany. *Flora* **201**, 233-239 (2006).

121. Leary, R. L. & Thomas, B. A. *Lepidodendron aculeatum* with attached foliage: evidence of stem morphology and fossilization processes. *Amer. J. Bot.* **76**, 283-288 (1989).

122. Lesquereux, L. On the Cordaites and their related generic divisions, in the Carboniferous Formation of the United States. *Proceed. Amer. Phil. Soc.* **17**, 315-335 (1878).

123. Wang, S.-J., Tian, B.-L., Chen, G.-R. Anatomically preserved lepidodendralean plants from Permian coal balls of China: leaves of *Lepidophylloides* Snigirevskaya. *Rev. Palaeobot. & Palynol.* **122**, 63-76 (2002).

124. Galtier, J. A new zygopterid fern from the Early Carboniferous of France and a reconsideration of the *Corynepteris-Alloiopteris* ferns. *Rev. Palaeobot. & Palynol.* **128**, 195-217 (2004).

125. DiMichele, W. A. & Phillips, T. The ecology of Paleozoic ferns. *Rev. Palaeobot. & Palynol.* **119**, 143-159 (2002).

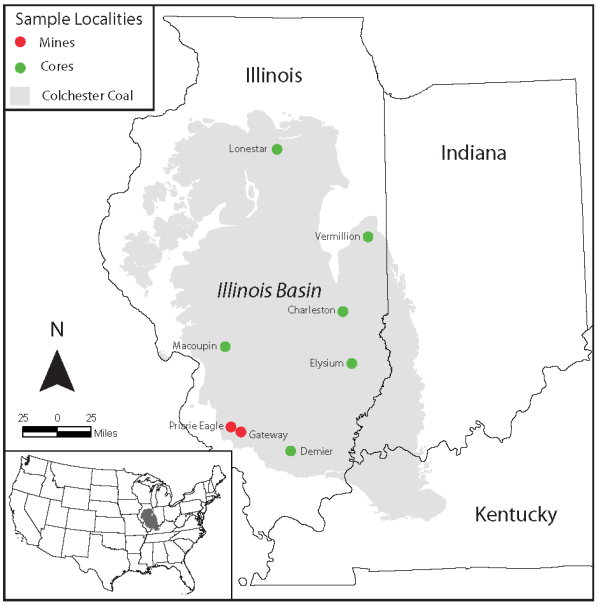

Supplementary Figure 1. Locality map for cores and mines sampled in the Illinois Basin. Gray shading delineates the geographic extent of the mid-Desmoinesian Colchester Coal.

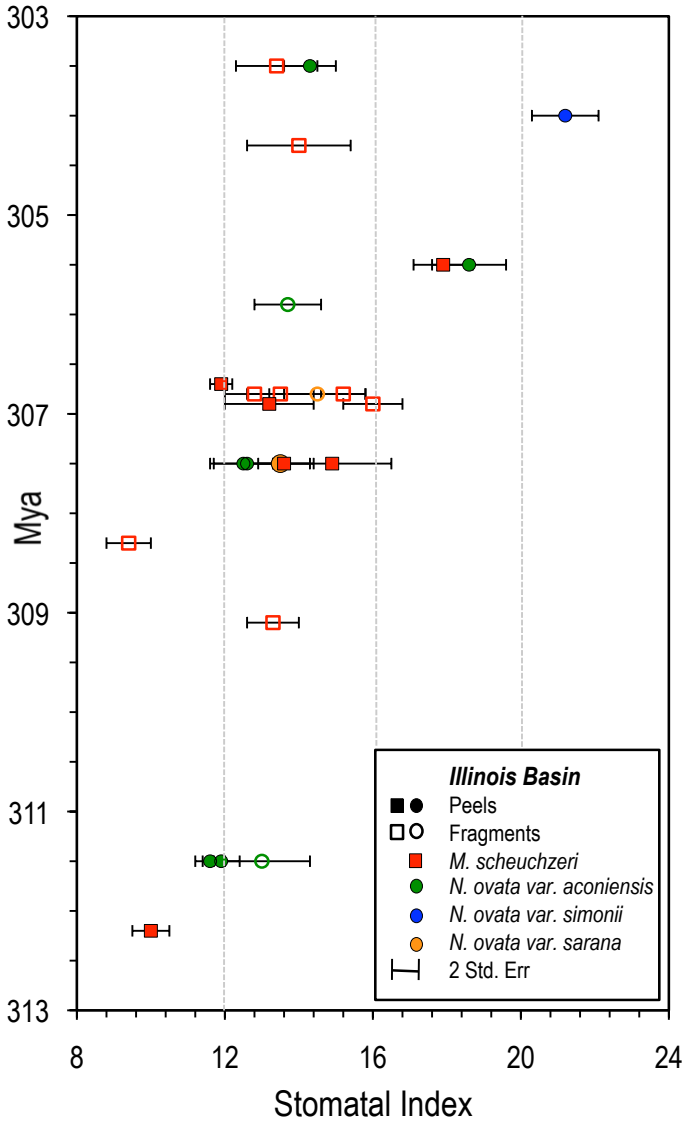

Supplementary Figure 2. Temporal distribution of cuticle SI values by taxa (coded by color) and material (macrofossil peel (closed symbols) or macerated fragments (open symbols)) over 13 cyclothems. Each data point is the mean value of counts for pinna collected from one plant bed; 2 standard error bars reflect intra- and inter-pinnule variability. Contemporaneous SI values exhibit the taxonomic and geographic variability across the basin.

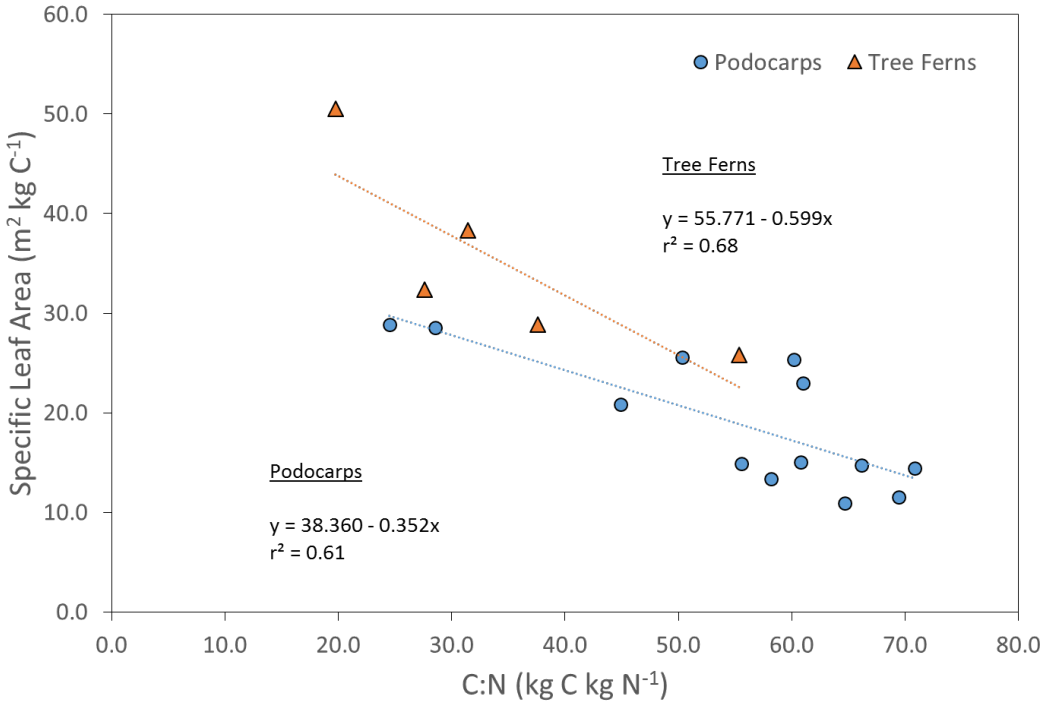

Supplementary Figure 3. Linear regression models for measured leaf C:N and specific leaf area (SLA) values for modern New Zealand Podocarpaceae and tree fern species derived from ref. *68*.

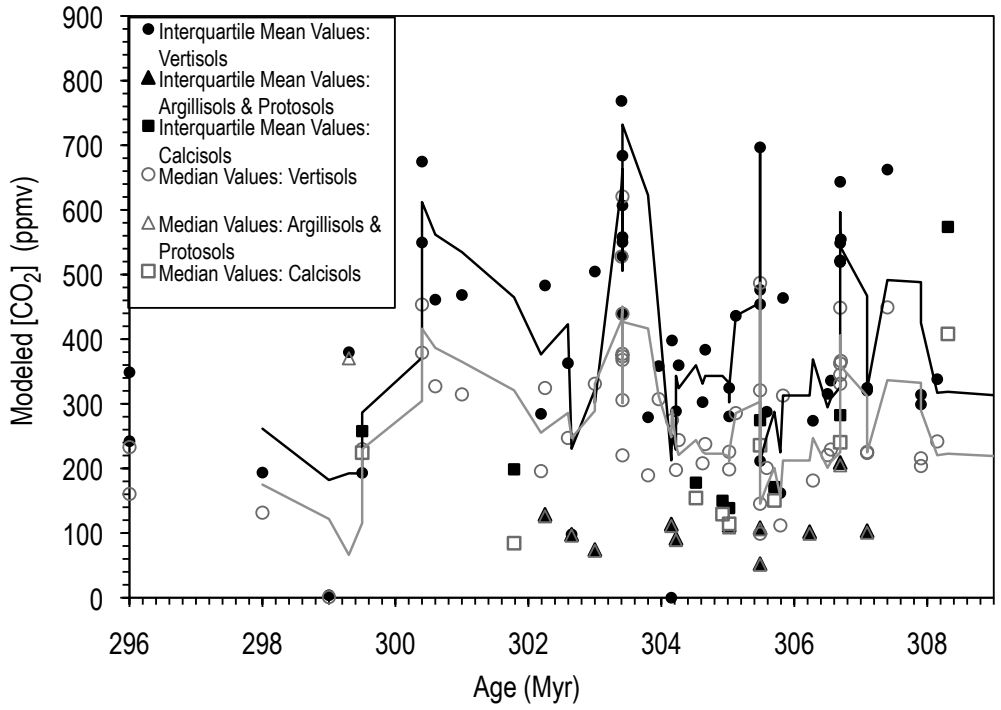

Supplementary Figure 4. Comparison of modeled best estimates of pCO_2, plotted by paleosol type and presented as median (open symbols) and interquartile mean (filled symbols) values. Trend lines are 3-pt running averages through the two sets of data.

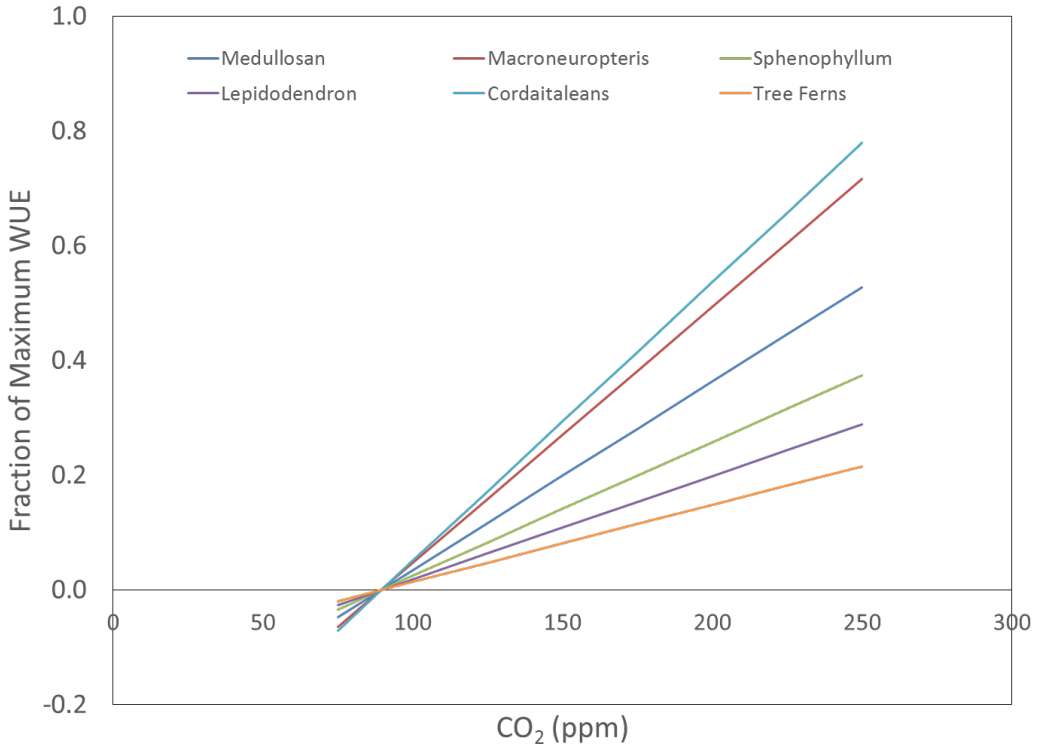

Supplementary Figure 5. Modeled fraction of maximum WUE for Carboniferous floral dominants over a pCO_2 range of 50 to 250 ppm. Results based on a Michaelis-Menten function analysis that permits linear extrapolation of WUE.

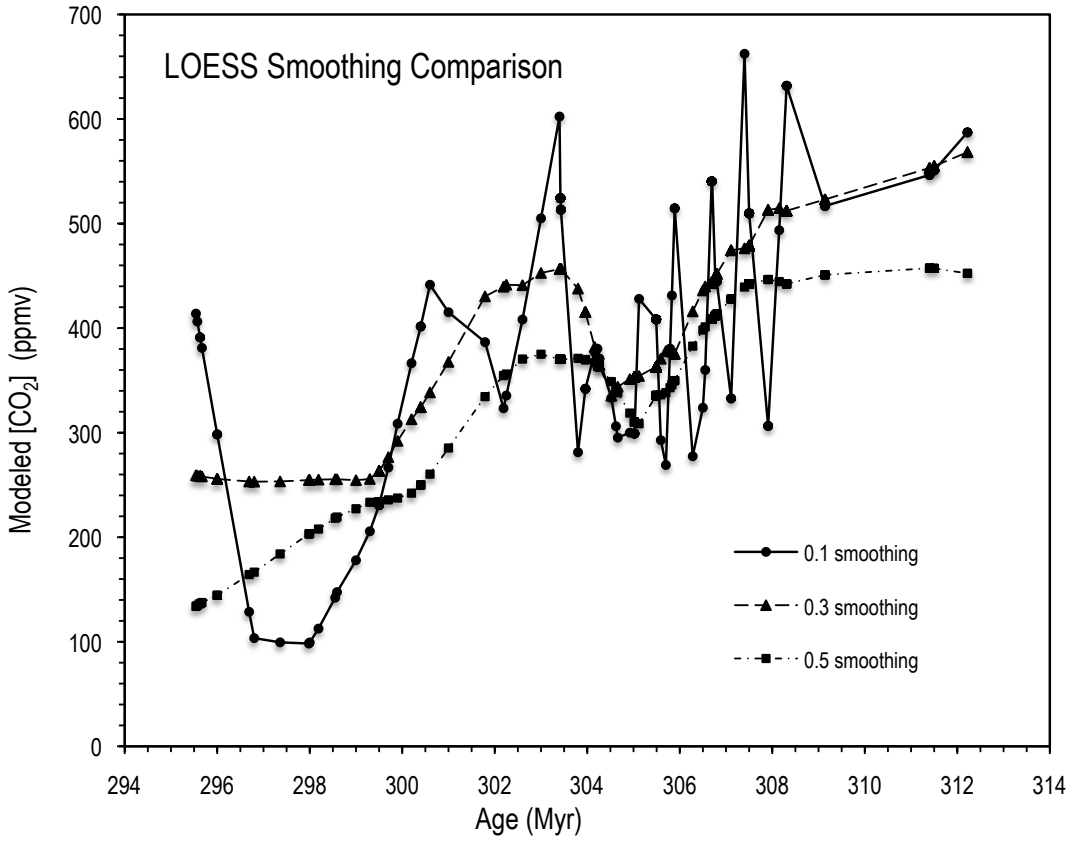

Supplementary Figure 6. Comparison of LOESS results from paleosol- and fossil plant-based CO_2 estimates using a 0.1, 0.3, or 0.5 smoothing parameter.

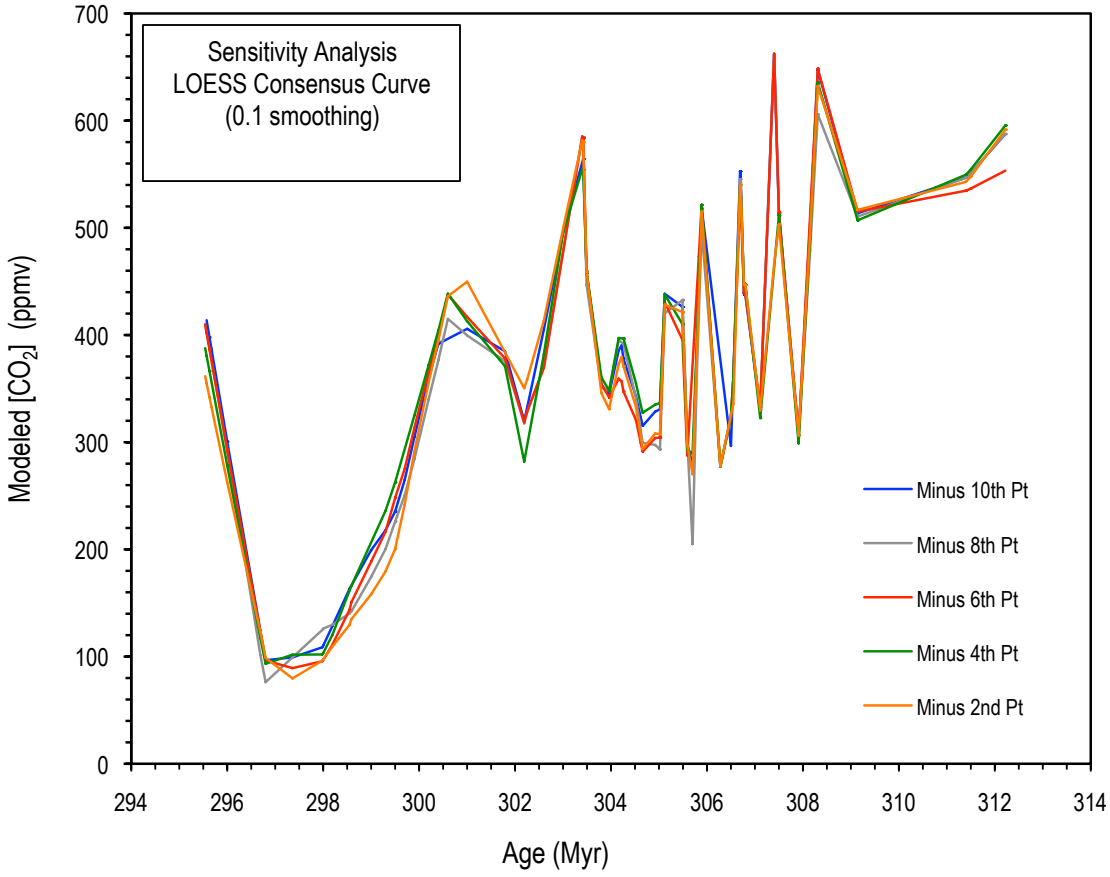

Supplementary Figure 7. Comparison of LOESS analysis of five different subsets of the full CO_2 data set. Consensus curves (0.1 smoothing) made using the integrated paleosol- and fossil leaf-based CO_2 dataset. Subsets were defined by excluding 10% of the data by removing every 10^{th} point beginning with the 2^{nd}, 4^{th}, 6^{th}, 8^{th}, or 10^{th} data point (Pt).

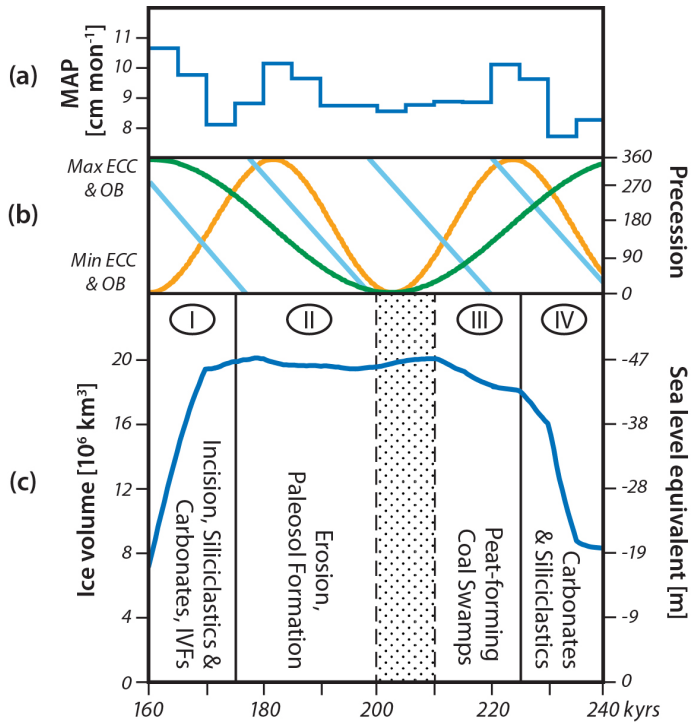

Supplementary Figure 8. Time series of (a) modeled Northern Hemisphere tropical terrestrial MAP, (b) orbital regime used for climate simulation (560 ppm CO_2), and (c) ice volume, glacioeustatic response, and depositional model through one eccentricity glacial-interglacial cycle. Ice sheet phase indicated as I: early glacial; II: peak glacial; III: late glacial; IV: deglaciation and interglacial. Stippled region bounded by dashed lines indicates the likely interval of transition from a dominantly erosive regime to peat accumulation. This reflects the point at which the rate of sea-level fall is outpaced by the regional subsidence rate, thus providing accommodation space for peat accumulation. Modified from ref. *78*.

Supplementary Table 1. Age model for the pCO_2 reconstruction and sample distribution.

Age[1] (Mya)	MCB[2]	Lithostratigraphic Units[3]	Midcontinent Major Cyclothem[4]	Major Coals (Illinois Basin)	Midcontinent Lithostrat. Equiv.[5]	Appalachian Basin Lithostrat. Equiv.[6]	Donets Basin Lithostrat. Equiv.[7]	Major IVF[8]	Samples (this study)[9]
298 - >296		Greene Fm, Dunkard (AB)							DUN 4-10; GRE 2 & 3
298 - 299.5		Washington Fm, Dunkard (AB)							1763:1-3; DUN 1-3; WASH 1
299.30		Q4 paleosols (DB)							KQ 11
299.5 - 300.5		Waynesburg A, Washington Fm, Dunkard (AB)							KV 180A
299.50		P5-1 paleosols (DB)							P5-1
300.40		P5 paleosols (DB)							
300.40		Monongahela Gp, Fishpot Lmst. (AB)							18902: 1-3
300.60		P4/5 paleosols (DB)							P4-P5
301.00		uppermost Conemaugh Gp (AB)							KV 182
301.79	MCB	Greenup Limestone			Topeka (Holt)		P2?	X	ELY 10
302.19	MCB	Shamrock & Newton Limestones			Deer Ck (Larsh)		P1		ELY 5; CHA 1; CH 3
302.60	MCB	Bogota Limestone	Lecompton		Lecompton Limestone	possibly the Gaysport	O7?		CH 8; CHA 2
303.00	MCB	Shumway Limestone	Oread		Oread Limestone	Ames Limestone	O6		CH 9; CHA 4
303.40		Conemaugh Gp: Pittsburgh Coal (AB)				Skelley			1712
303.45	MCB	Omega Limestone	Cass		Cass Limestone		O5		
303.55		Harlem Coal (AB)				Harlem			G9HarlRHz 1-3; H 22 HC-PRB 1-4; P1-P6
303.70		*proposed Kasim-Gzhelian bdry (in Heebner Shale)*							
303.70		*Missourian-Virgilian bdry (base of Cass cycle)*						X	
303.76		Calhoun & Shelbyville coals							fossil plants
303.80		Little Vermillion Limestone			Stanton Limestone	Noble/Mill Ck lmsts.	O4-6H		CH 13
303.84	MCB	Eudora Shale (MC)	Stanton						
303.96		Cohn & McCleary's Bluff coals							ELY 30-32; fossil plants
304.13		U. Millersville-La Salle-Livingston Limestone	limestone unit split into 3 parts:top		Iola Limestone				CHA 8
304.16		Friendsville Coal	between 2nd & 3rd part of limestone unit						ELY 36, 37
304.22		L. Millersville-La Salle-Livingston Lmst.	limestone unit split into 3 parts:bottom		Iola Limestone				CH 16 & 21
304.25	MCB	Muncie Creek Shale (MC)	Iola				O4-3H		
304.26		Bristol Hill Coal				Portersville/Woods Run			ELY 42 & 44; fossil plants
304.42		Coffeen Limestone							
304.45		Flannigan Coal							
304.52		Reel Limestone							ELY 48

Supplementary Table 1. Age model for the pCO_2 reconstruction and sample distribution.

Age[1] (Mya)	MCB[2]	Lithostratigraphic Units[3]	Midcontinent Major Cyclothem[4]	Major Coals (Illinois Basin)	Midcontinent Lithostrat. Equiv.[5]	Appalachian Basin Lithostrat. Equiv.[6]	Donets Basin Lithostrat. Equiv.[7]	Major IVF[8]	Samples (this study)[9]
304.62		Hall Limestone			Dewey Limestone				LSC 17 & 21
304.65	MCB	Quivira Shale (MC)	Dewey				O4-1	X	
304.66		Flat Ck Coal				Cambridge/Nadine lmsts.			CHA 10; CH 25
304.82		Sorento Limestone			Cherryvale Fm		O3		
304.88		Fairbanks Coal							
305.02		Carthage Limestone				Upper Brush Ck			LSC 11, 12, 14, 24, 64; CH 29, 32; CHA 11 & 14
305.06	MCB	Shoal Ck	Dennis		Dennis Lmst. (Stark Shale)	Pine Ck	O2	X	
305.07		New Haven Coal							
305.43		Macoupin Limestone			Swope Limestone	Lower Brush Ck			
305.46	MCB	Hushpuckney Shale (MC)	Swope				O1		
305.49		Womac coal (end hypothesized strat. gap (Wagner & Lyons 1997))		Womac					ELY 66 & 68; MAC 10; VER 2-4, 8, 9; CHA 16; CH 35; fossil plants
305.70		Carlinville Limestone					N5-2?		MAC 8
305.73		Cramer Limestone			Hertha Limestone				
305.76	MCB	Mound City Shale (MC)	Hertha				N5-1		
305.79		Chapel coal		Chapel					LSC 5; fossil plants
305.83		Exline Limestone (prev. Scottsville); upper West Franklin Lmst.	*Possible base of Kasimovian*		Exline Limestone		N5		ELY 57A
305.86		*MAJOR FLORAL STEP CHANGE*							
305.89		Athensville Coal		Athensville Coal (#8)	Checkerboard S-Md	Mason Coal			fossil plants
306.00		*Desmoinesian-Missourian Bdry*							
306.10	MCB	Seminole Sandstone	Lost Branch					XX	
306.23		Lonsdale Limestone (midddle West Franklin Limestone)			Lost Branch Fm		N3-3 (306.08)		LSC 36
306.28		Atilla Shale							MAC 26 & 28
306.29		Rock Branch Coal			Dawson Coal	Mahoning Coal		X	
306.31	MCB	Gimlet Sandstone (&widespread paleosol)	Altamont	(beginning of hypothesized stratigraphic gap (Wagner and Lyons, 1997))				XX	
306.40		De Graff Coal		possibly equiv to Pirtle					
306.50		Piasa Limestone (lower West Franklin Limestone)			Altamont Limestone		N3-1		CHA 18-20; LSC 4, 36
306.60		Farmington Shale	*Current correlated base of Kasimovian*		Farlington Shale		N3		

Supplementary Table 1. Age model for the pCO_2 reconstruction and sample distribution.

Age[1] (Mya)	MCB[2]	Lithostratigraphic Units[3]	Midcontinent Major Cyclothem[4]	Major Coals (Illinois Basin)	Midcontinent Lithostrat. Equiv.[5]	Appalachian Basin Lithostrat. Equiv.[6]	Donets Basin Lithostrat. Equiv.[7]	Major IVF[8]	Samples (this study)[9]
306.78		Cottage Coals (n=2)							fossil plants (3 intervals)
306.80		Baker		Baker		Upper Freeport leader coal	possibly equiv. to N2-1		fossil plants (2 intervals)
306.83		Bankston Fork Limestone			Coal City Limestone?				
307.09		Anna Shale			Anna Shale	Dorr Run	N2 B		
307.10	MCB	Herrin Coal	Pawnee	Herrin (#6 coal)		Lower Freeport coal/U. Kittaning	just below N2H		CHA 25; CH 43; GAT 3-5, 16-18; PEM 2-4; fossil plants
307.42	MCB	St. David Limestone	Upper Ft. Scott		Little Osage Shale	Washingtonville Shale	N1-7 to N1-8		
307.40		N1—N2 lmsts, paleosols (DB)							N1-N2: 1-8
307.50		Springfield Coal		Springfield (#5 coal)	Summit	Middle Kittaning coal	possibly equiv. to N1-5		fossil plants (2 intervals)
307.52	MCB	Galatia Sandstone	Lower Ft Scott				N1-4 ish range		
307.86		Excello Shale			Excello Shale	Washingtonville Shale	N-1 to N1-4 range		N1-N2 (Donets)
307.91	MCB	Houchin Creek Coal	(Bevier??						ELY 106; MAC 59
308.15		Survant Coal							MAC 56
308.28		Mecca Quarry Shale (Francis Ck Shale)			Verdigris Limestone (Oakley Sh.)		M9		
308.31	MCB	Colchester Coal	Verdigris	Colchester		Lower Kittaning coal			LSC 54; fossil plants
308.75		Palzo Sandstone							
309.14		Seelyville Coal		Seeleyville					fossil plants
309.70	MCB	Carner Mills Shale	Upper Tiawah				M7 (S&D, 2012)		
310.90	MCB	Seahorne or Stonefort Limestone	Inola		Inola Limestone		between M2 & 3		
311.10		Mt Rorah		Mt Rorah					fossil plants
311.50		Murphysboro Coal		Murphysboro					fossil plants
312.00	MCB	Mitchellsville Limestone	possibly equiv. to Doneley						
311.90		Kanawha: Mercer (AB)							
312.00		*Atokan—Desmoinesian boundary*	Bell Coal						
312.20	MCB	Curlew (Seville) Limestone	possibly equiv. to McCurtain						
312.22		Upper Block Rider Coal							fossil plants

[1]Ages based on Pennsylvanian stage boundaries[65] assuming an age of 312 Ma for the Desmoinesian-Atokan boundary and a 405 kyr duration for major cyclothems in the Midcontinent and Illinois Basin[11], and on cyclothem correlations and age assignments[60].

[2]MCB = major cyclothem (405 kyr) boundaries in the Midcontinent as defined by ref. *11* and citations within.

[3]All lithostratigraphic units (and associated samples) other than those from the Illinois Basin are indicated as MC (Midcontinent), AB (Appalachian Basin), and DB (Donets Basin)

[4]Major cyclothems of Heckel[11] modified slightly based on unpublished data of P. Holterhoff (pers. comm. 2015)

[5]Correlation of Illinois Basin cyclothems to the Midcontinent cyclothems using limestone and shale marker units is based on refs. *11* and *58*.

[6]Correlation of Illinois Basin cyclothems to the Appalachian Basin cyclothems using limestones and coals is based on ref. *11* and citations within.

[7]Correlation of Illinois Basin cyclothems to the Donets Basin cyclothems after refs. 58-60.

[8]Stratigraphic distribution of major incised valley fills (IVF) as defined by refs. 11, 19, and 58. Double X indicates deepest incision channels in succession (>30 to 40+ m)[19]. Note: IVF underlie limestone units for which Midcontinent cyclothems are named.

[9]Core location (see Supplementary Fig. 1) of samples indicated by: Lonestar (LSC), Vermillion (VER), Charleston (CH & CHA), Elysium (ELY), Macoupin (MAC), Gateway (GAT), Demier (DEM)

Supplementary Table 2. Input variables for PBUQ and modeled CO_2 based on pedogenic carbonates

[1]Age (Mya)	Sample (n)	[2]Stratigraphic Marker Bed or Unit	Soil Order/type	Pedogenic $\delta^{13}C_{carb}$ ‰	(± 1σ)	[3]Respired CO_2 $\delta^{13}C$: discrete org ‰	(± 1σ)
*300.2	HT 1-3, (7)	Honaker Trail Fm, UT	sandy Calcisols	-3.4	0.6	-20.5	1.0
*299.9	N1: 1-2, (2)	Hermit Shale Fm, Kohl's Ranch, AZ	Calcisols	-4.2	1.1	-20.5	1.0
*299.7	BF 1-7, (5)	Bursum Fm, Socorro, NM	Calcisols	-6.1	0.3	-21.0	1.1
*299.5	HAL 1-4, 7, 9, 12, 17, 18, 22, 25-26, 48, (16)	upper Halgaito Fm, AZ	silty Calcisols	-4.0	0.2	-20.5	0.8
*298.6	S4, (3)	Hermit Shale Fm, Flagstaff, AZ (upper set)	muddy Calcisols	-5.4	0.2	-20.5	0.8
*298.5	S2, (2)	Hermit Shale Fm, Flagstaff, AZ (lower set)	muddy Calcisols	-6.7	0.1	-20.5	0.8
*298.2	AC 31-32, (2)	middle Archer City Fm, stratotype (SS5), nc-TX	calcic Vertisols	-7.1	1.5	-21.3	0.5
*298.0	ABBA 3-9; ACBBH/R, (4)	upper Archer City Fm bonebed (SS8), nc-TX	Alfisols	-9.4	1.0	-21.3	0.5
*297.4	NBC2 & 4, (3)	basal Nocona Fm, coprolite bonebed, nc-TX	calcic Vertisols	-9.5	1.0	-21.3	1.1
*296.8	NLAD 2 & 99	middle Nocona Fm, nc-TX	calcic Vertisols	-8.6	0.8	-21.3	1.1
*296.7	A 3-10, (11)	Abo Fm, Socorro to Las Cruces, NM	calcic Vertisols	-5.6	0.6	-21.4	0.7
296.0	Dunkard 4-10, (12)	Greene Fm, Dunkard Gp. Appal. Basin	calcic Vertisols	-8.9	1.2	-24.5	1.0
296.0	GRE 2 & 3, (4)	Greene Fm, Dunkard Gp. Appal. Basin	calcic Vertisols	-8.0	0.3	-24.5	1.0
298.0	DUN 1-3, (6)	Washington Fm, Dunkard Gp. Appal. Basin	calcic Vertisols	-9.0	0.5	-24.1	0.4
299.0	WASH 1, (2)	Washington Fm, Dunkard Gp. Appal. Basin	calcic Vertisols	-11.7	0.0	-24.1	0.4
299.3	KQ 11, (8)	Q4 Limestone, Donets Basin	Argillisol	-6.4	0.1	-23.8	0.3

[1]Age (Mya)	Sample (n)	[2]Stratigraphic Marker Bed or Unit	Soil Order/type	Pedogenic $\delta^{13}C_{carb}$ ‰	(± 1σ)	[3]Respired CO_2 $\delta^{13}C$: discrete org ‰	(± 1σ)
299.5	1763: 1-3, (5)	Washington Fm, Dunkard Gp. Appal. Basin	calcic Vertisols	-10.3	1.1	-23.6	0.5
299.5	P5-1, (2)	P5-1 Limestone, Donets Basin	Calcisol	-6.9	0.5	-23.8	0.3
300.4	KV180A (2)	Waynesburg Fm, Dunkard Gp, Appal. Basin	calcic Vertisol	-6.5	0.1	-23.8	0.3
300.4	18902, (8)	Monongahela Gp, Fishpot Lmst. Appal. Basin	Vertisol	-7.3	0.5	-24.2	0.5
300.6	P4-P5, (2)	P4 & P5 limestones, Donets Basin	calcic Vertisol	-7.0	0.4	-23.8	0.3
301.0	KV182: 1 & 2, (2)	upper Conemaugh Gp, Appal. Basin	calcic Vertisol	-7.0	0.6	-23.8	0.3
301.8	ELY 10, (4)	Greenup Limestone, Illinois Basin	Calcisol	-7.4	0.3	-23.1	0.4
302.2	ELY 5, (6)	Shamrock/Newton Lmst, , Illinois Basin	gleyed calcic Vertisol	-7.5	0.1	-23.1	0.4
302.3	CHA 1, (2)	Newton Lmst., Illinois Basin	gleyed calcic Vertisol	-6.5	0.1	-23.7	0.2
302.3	CH 3, (1)	Newton Lmst., Illinois Basin	gleyed calcic Protos	-6.8	0.1	-23.7	0.1
302.6	CH 8, (4)	Bogata Lmst., Illinois Basin	gleyed calcic Vertisol	-7.3	0.3	-23.7	0.2
302.7	CHA 2, (2)	Bogata Lmst., Illinois Basin	gleyed calcic Protosol	-7.5	0.1	-23.7	0.2
303.0	CHA 4, (4)	Shumway Lmst., Illinois Basin	gleyed calcic Vertisol	-6.5	0.3	-23.7	0.2
303.0	CH 9, (3)	Shumway Lmst., Illinois Basin	gleyed calcic Protosol	-8.2	0.4	-23.7	0.2
303.4	1712, (7)	Conemaugh Gp, Pittsburgh Coal, Appal. Basin	calcic Vertisols	-5.2	0.3	-23.1	0.2
303.4	G9HarlRHz 1-3, (6)	Conemaugh Gp, Harlem Coal, Appal. Basin	calcic Vertisols	-6.0	0.2	-23.6	0.5
303.4	H22, (2)	Conemaugh Gp, Harlem Coal, Appal. Basin	calcic Vertisols	-6.1	0.0	-23.6	0.5

[1]Age (Mya)	Sample (n)	[2]Stratigraphic Marker Bed or Unit	Soil Order/type	Pedogenic $\delta^{13}C_{carb}$ ‰	(± 1σ)	[3]Respired CO_2 $\delta^{13}C$: discrete org ‰	(± 1σ)
303.4	HC-PRB-1-4, (12)	Conemaugh Gp, Harlem Coal, Appal. Basin	calcic Vertisols	-6.7	0.5	-23.6	0.5
303.4	P1-1-5, (8)	Conemaugh Gp, Harlem Coal, Appal. Basin	calcic Vertisol	-6.0	0.2	-23.6	0.5
303.4	P5-1-4, (5)	Conemaugh Gp, Harlem Coal, Appal. Basin	calcic Vertisol	-5.5	1.0	-23.6	0.5
303.4	P3-1-5, (11)	Conemaugh Gp, Harlem Coal, Appal. Basin	calcic Vertisol	-5.6	0.8	-23.6	0.5
303.4	P6-1-5, (8)	Conemaugh Gp, Harlem Coal, Appal. Basin	calcic Vertisol	-6.9	0.2	-23.6	0.5
303.8	CH 13, (2)	Little Vermillion Lmst., Illinois Basin	gleyed calcic Vertisol	-8.7	0.1	-24.5	0.5
304.0	ELY 30-32, (5)	Cohn Coal, Illinois Basin	gleyed calcic Vertisol	-8.1	0.3	-24.5	0.5
304.1	CHA 8, (3)	Millersville Lmst., Illinois Basin	calcic Protosol	-8.1	0.2	-24.1	0.3
304.2	ELY 36 & 37, (4)	Friendsville Coal, Illinois Basin	gleyed calcic Vertisol	-7.7	0.9	-24.5	0.5
304.2	CH 16, (4)	Lower Millersville Lmst., Illinois Basin	gleyed calcic Vertisol	-8.3	0.2	-24.1	0.3
304.2	CH 21, (3)	Lower Millersville Lmst., Illinois Basin	gleyed calcic Protosol	-8.1	0.4	-24.1	0.3
304.3	ELY 44 & 42, (4)	Bristol Coal, Illinois Basin	gleyed calcic Vertisol	-8.0	0.6	-24.5	0.5
304.5	ELY 48, (2)	Reel Lmst., Illinois Basin	gleyed Calcisol	-8.9	0.0	-25.3	0.7
304.6	LSC 17 & 21, (6)	Lower Hall Lmst, Illinois Basin	calcic Vertisol	-8.4	0.3	-25.0	1.0
304.7	CH 25 & CHA 10, (6)	Flat Creek Coal, Illinois Basin	gleyed calcic Vertisol	-8.2	0.5	-24.6	1.1
304.9	CH 29, (4)	above Carthage Lmst, Illinois Basin	gleyed Calcisol	-8.3	0.1	-24.0	1.2
305.0	LSC 11-12, 14, (6)	Carthage Lmst., Illinois Basin	Vertisol	-8.2	0.3	-24.0	1.0

[1]Age (Mya)	Sample (n)	[2]Stratigraphic Marker Bed or Unit	Soil Order/type	Pedogenic $\delta^{13}C_{carb}$ ‰	(± 1σ)	[3]Respired CO_2 $\delta^{13}C$: discrete org ‰	(± 1σ)
305.0	CHA 11 & CH 29, (8)	Carthage Lmst., Illinois Basin	Protosol	-7.4	0.0	-24.0	1.2
305.0	CHA 14 & CH 32, (2)	Carthage Lmst., Illinois Basin	gleyed Calcisol	-8.5	1.0	-24.0	1.2
305.1	LSC 24, (2)	below Carthage Lmst, Illinois Basin	calcic Vertisol	-7.6	0.0	-24.0	1.0
305.5	MAC 12, (2)	Womac Coal, Illinois Basin	gleyed calcic Vertisol	-7.0	0.0	-24.1	0.3
305.5	LSC 36, (5)	Womac Coal, Illinois Basin	gleyed calcic Vertisol	-7.0	0.1	-23.8	1.0
305.5	ELY 68 & 66, (4)	Womac Coal, Illinois Basin	gleyed vertic Calcisol	-7.1	1.0	-24.3	0.2
305.5	CHA 16 & CH 35, (2)	Womac Coal, Illinois Basin	gleyed calcic Protosol	-9.4	0.2	-24.1	0.2
305.5	VER 8, (3)	Womac Coal, Illinois Basin	gleyed calcic Vertisol	-9.1	0.5	-24.1	0.3
305.5	VER 9, (2)	Womac Coal, Illinois Basin	gleyed calcic Protosol	-8.5	0.0	-24.1	0.3
305.6	VER 2 to 4, (6)	below Womac Coal, Illinois Basin	gleyed calcic Vertisol	-8.4	0.6	-24.1	0.3
305.7	MAC 8, (2)	Carlinsville Lmst., Illinois Basin	gleyed vertic Calcisol	-8.0	0.2	-24.0	1.0
305.8	LSC 5, (4)	Chapel Coal, Illinois Basin	gleyed calcic Vertisol	-9.4	0.0	-24.0	1.0
305.8	ELY 57A, (1)	Exline Lmst., Illinois Basin	gleyed Vertisol	-6.6	0.1	-23.3	0.1
306.2	LSC 36, (1)	middle W. Franklin Lmst., Illinois Basin	gleyed calcic Protosol	-7.8	0.1	-24.0	1.0
306.3	MAC 28 & 26, (3)	Atilla Shale/Rockbranch, Illinois Basin	gleyed Vertisol	-7.6	0.1	-23.0	1.0
306.5	CHA 18-20, (7)	Piasa Lmst., Illinois Basin	gleyed calcic Vertisol	-8.5	0.4	-24.6	1.0
306.6	LSC 4, (2)	lower W. Franklin Lmst., Illinois Basin	gleyed calcic Vertisol	-8.7	0.0	-24.0	1.0

[1]Age (Mya)	Sample (n)	[2]Stratigraphic Marker Bed or Unit	Soil Order/type	Pedogenic $\delta^{13}C_{carb}$		[3]Respired CO_2 $\delta^{13}C$: discrete org	
				‰	(± 1σ)	‰	(± 1σ)
306.7	MAC 46, (2)	Danville Coal, Illinois Basin	gleyed vertic Calcisol	-6.2	0.1	-23.3	1.0
306.7	ELY 81 & 83, (4)	Danville Coal, Illinois Basin	gleyed calcic Vertisol	-6.1	0.8	-23.5	2.0
306.7	CHA 23, (2)	Danville Coal, Illinois Basin	calcic Protosol	-6.0	0.4	-23.3	1.0
306.7	LSC 40 & 39, (2)	Danville Coal, Illinois Basin	Calcic Vertisol	-5.5	0.2	-23.1	0.6
306.7	CH 41, (4)	Danville Coal, Illinois Basin	gleyed calcic Vertisol	-6.4	0.5	-23.7	0.4
306.7	LSC 38, (3)	below Danville Coal, Illinois Basin	gleyed calcic Vertisol	-7.4	0.4	-23.1	0.6
307.1	GAT 3-5, 16-18, (14)	Herrin Coal, Illinois Basin	calcic Vertisol	-8.5	0.8	-23.5	1.0
307.1	PEM 2-4, (6)	Herrin Coal, Illinois Basin	Vertisol	-8.0	0.2	-24.0	1.0
307.1	CH 43 & CHA 25, (4)	Herrin Coal, Illinois Basin	gleyed calcic Protosol	-8.1	0.7	-24.4	0.1
307.4	N1-N2 (5)	mid pt of N1-N2 lmsts, Donets Basin	gleyed calcic Vertisol	-5.6	0.6	-24.0	0.5
307.9	ELY 106, (2)	Houchin Ck Coal, Illinois Basin	gleyed Calcic Vertisol	-8.3	0.1	-24.5	0.4
307.9	MAC 59, (2)	Houchin Ck Coal, Illinois Basin	gleyed calcic Vertisol	-8.4	0.0	-24.5	1.0
308.2	MAC 56, (2)	Survant Coal, Illinois Basin	gleyed calcic Vertisol	-7.7	0.1	-24.1	0.7
308.3	LSC 54, (5)	Cochester Coal, Illinois Basin	gleyed vertic Calcisol	-5.4	0.5	—	—

[1]Samples marked by an '*' are from Montañez et al.(*ref.* 30); revised CO_2 estimates were defined using PBUQ.

[2]Stratigraphic units are closest marker unit for reference or formation/group in which the samples were collected; ages within a formation/group or above/below a marker bed were interpolated based on meterage and biostratigraphic tie-points. See Supplementary Table 1 for full stratigraphic context.

[3]See Methods for details of how soil-respired CO_2, presented in this table, was estimated from discrete and occluded organic matter.

[4]For the previously published samples from north-central TX (4 marked by an '*'), MAATs were constrained using values from ref. 25 as follows:

(1) for proxy soil temperatures > 30°C, then MAAT 5°C lower, (2) for proxy soil temperatures >25°C to ≤ 30°C, then MAAT 3°C lower, and (3) for proxy soil temperatures ≤ 25°C, then MAAT = soil temperature. MAATs for samples from AZ, NM, and UT were similarly assigned based on stratigraphic equivalent intervals from TX.

[5]Best estimate of pCO_2 based on trimmed mean. For those samples for which the $\delta^{13}C$ of the organic matter occluded in pedogenic carbonates was analyzed, the best estimate pCO_2 utilized those input values.

[6]An alternative *p*CO2 estimate, based on the $\delta^{13}C$ of discrete organic matter closely associated with the paleosol, is provided for those samples for which soil-respired CO_2 was constrained by both discrete and occluded organic matter.

Supplementary Table 2.

[3]Respired CO_2 $\delta^{13}C$: occlud. org		[4]Temp. °C	Marine $\delta^{13}C_{carb}$		[5]Best Estimate CO_2	16%	84%	[6]Alt. Estimate CO_2 (16/84 %)
‰	(± 1σ)	(± 3°)	‰	(± 1σ)	ppm	ppm	ppm	ppm
—	—	24.0	4.6	0.2	331	128	695	
—	—	24.0	4.6	0.2	247	76	548	
—	—	24.0	4.7	0.2	128	37	287	
—	—	24.0	4.7	0.2	290	117	590	—
—	—	26.0	4.8	0.2	169	66	350	—
—	—	26.0	4.8	0.2	83	21	186	—
—	—	26.0	4.8	0.2	158	10	519	—
—	—	30.0	4.9	0.2	10	1	49	—
—	—	29.0	4.9	0.2	14	1	78	—
—	—	28.0	4.4	0.2	47	1	183	—
—	—	28.0	4.4	0.2	404	101	1162	—
—	—	23.0	3.9	0.5	242	46	734	—
—	—	23.0	3.9	0.5	349	85	996	—
—	—	23.0	4.2	0.5	194	47	558	—
—	—	23.0	4.2	0.5	4	1	19	—
—	—	23.0	2.8	0.7	380	270	527	—

[3]Respired CO_2 $\delta^{13}C$: occlud. org		[4]Temp. °C	Marine $\delta^{13}C_{carb}$		[5]Best Estimate CO_2	16%	84%	[6]Alt. Estimate CO_2 (16/84 %)
‰	(± 1σ)	(± 3°)	‰	(± 1σ)	ppm	ppm	ppm	ppm
-24.3	0.2	23.0	2.8	0.7	193	42	569	69 (1/265)
—	—	23.0	2.8	0.7	258	106	528	—
—	—	23.0	2.8	0.7	550	139	1573	—
-25.4	0.2	23.0	3.9	0.3	675	168	1902	450 (111/1291)
—	—	23.0	2.8	0.7	461	116	1318	—
—	—	23.0	3.0	0.5	468	116	1339	—
—	—	23.0	3.8	0.3	199	57	406	—
—	—	23.0	3.9	0.3	284	72	817	—
—	—	23.0	3.9	0.3	483	117	1389	—
—	—	23.0	3.9	0.3	129	85	184	—
—	—	23.0	4.0	0.4	363	92	1033	—
—	—	23.0	4.0	0.4	98	63	141	—
—	—	23.0	4.0	0.4	505	122	1449	—
—	—	23.0	4.0	0.4	74	45	110	—
-23.0	0.2	23.0	3.9	0.4	769	192	2195	645 (162/1846)
—	—	23.0	3.9	0.4	558	138	1607	—
—	—	23.0	3.9	0.4	528	132	1508	—

[3]Respired CO_2 $\delta^{13}C$: occlud. org		[4]Temp. °C	Marine $\delta^{13}C_{carb}$		[5]Best Estimate CO_2	16%	84%	[6]Alt. Estimate CO_2 (16/84 %)
‰	(± 1σ)	(± 3°)	‰	(± 1σ)	ppm	ppm	ppm	ppm
—	—	23.0	3.9	0.4	440	112	1260	—
—	—	23.0	3.9	0.4	550	139	1593	—
—	—	23.0	3.9	0.4	607	114	2305	—
-25.1	0.2	23.0	3.9	0.4	905	228	2535	609 (153/1732)
-25.1	0.2	23.0	3.9	0.4	684	165	1960	415 (103/1182)
—	—	23.0	3.9	0.4	279	70	800	—
—	—	23.0	3.9	0.4	358	82	990	—
-24.0	0.2	23.0	3.8	0.4	114	72	165	90 (58/131)
—	—	23.0	3.8	0.4	398	98	1131	—
—	—	23.0	3.6	0.4	289	73	827	—
—	—	23.0	3.6	0.4	92	57	134	—
—	—	23.0	3.6	0.4	360	89	1048	—
—	—	23.0	3.5	0.5	178	75	364	—
-23.3	0.2	23.0	3.5	0.5	303	76	868	351 (89/1017)
-23.5	0.2	23.0	3.5	0.5	395	84	971	349 (83/1021)
—	—	23.0	3.4	0.5	150	52	319	—
—	—	23.0	3.4	0.5	281	67	807	—

[3]Respired CO_2 $\delta^{13}C$: occlud. org		[4]Temp. °C	Marine $\delta^{13}C_{carb}$		[5]Best Estimate CO_2	16%	84%	[6]Alt. Estimate CO_2 (16/84 %)
‰	(± 1σ)	(± 3°)	‰	(± 1σ)	ppm	ppm	ppm	ppm
—	—	23.0	3.4	0.5	112	62	175	—
—	—	23.0	3.4	0.5	139	36	314	—
—	—	23.0	3.3	0.5	436	108	1230	—
—	—	23.0	3.2	0.5	476	119	1356	—
—	—	23.0	3.1	0.5	454	109	1293	—
—	—	23.0	3.1	0.5	275	107	569	—
—	—	23.0	3.1	0.5	52	31	79	—
—	—	23.0	3.1	0.5	212	52	623	—
—	—	23.0	3.1	0.5	108	69	156	—
—	—	23.0	3.1	0.5	288	71	833	—
—	—	23.0	3.1	0.5	171	67	356	—
-22.9	0.2	23.0	3.1	0.5	162	38	477	158 (32/462)
—	—	23.0	3.1	0.5	464	116	1324	—
—	—	23.0	3.1	0.5	102	57	159	—
—	—	23.0	3.1	0.5	274	63	788	—
—	—	23.0	3.1	0.5	315	77	904	—
-23.9	0.2	23.0	3.1	0.5	336	83	968	241 (56/695)

[3]Respired CO_2 $\delta^{13}C$: occlud. org		[4]Temp. °C	Marine $\delta^{13}C_{carb}$		[5]Best Estimate CO_2	16%	84%	[6]Alt. Estimate CO_2 (16/84 %)
‰	(± 1σ)	(± 3°)	‰	(± 1σ)	ppm	ppm	ppm	ppm
—	—	23.0	3.1	0.5	282	115	574	—
—	—	23.0	3.1	0.5	519	38	1622	—
-23.6	0.2	23.0	3.1	0.5	209	132	307	162 (85/247)
—	—	23.0	3.1	0.5	643	160	1836	—
—	—	23.0	3.1	0.5	549	138	1591	—
-24.3	0.2	23.0	3.1	0.5	640	137	1583	322 (79/928)
-23.7	0.2	23.0	3.2	0.5	325	80	938	251 (39/612)
-22.9	0.2	23.0	3.2	0.5	321	81	916	319 (80/924)
—	—	23.0	3.2	0.5	104	60	159	—
—	—	23.0	4.0	0.6	662	167	1886	—
—	—	23.0	4.0	0.6	314	79	893	—
—	—	23.0	4.0	0.6	299	73	849	—
—	—	23.0	4.1	0.6	338	88	951	—
-23.8	0.2	23.0	4.1	0.6	644	157	1213	—

Supplementary Table 3. Measured input variables for fossil leaf-based proxies and resulting pCO_2

Age	Associated Coal	Sample ID	Taxa	Stomatal Index		Stomat. Density		Stomat. Length	
(Mya)		[1](stomatal box counts)		mean	± 2 Std. Err.	mean	± 2 Std. Err.	mean	± 2 Std. Err.
303.5	Calhoun Coal (floor)	38883 (12)	*M. scheuchzeri*	13.4	1.1	189	22	27.5	0.7
303.5	Calhoun Coal	38324 (9)	*N. ovata, var. acon.*	14.3	0.7	221	14	36.3	< 0.001
304.0	Cohn Coal (roof shale)	FN III-40 (68)	*N. ovata, simonii*	21.2	0.9	277	20	30.3	0.2
304.3	Bristol Hill Coal	38359 (8)	*M. scheuchzeri*	14.0	1.4	199	29	24.8	0.9
305.5	Womac Coal	1993-4 (27)	*N. ovata, var. acon.*	18.6	1.0	206	12	31.7	< 0.001
305.5	Womac Coal	1993-4: PZ-228 (23)	*M. scheuchzeri*	17.9	0.8	207	31	31.5	1.1
305.9	Athensville Lake Creek Coal	FNIX:99-101 (9)	*N. ovata, var. acon.*	13.7	0.9	199	21	20.6	0.3
306.7	Danville Coal (roof shale)	FN VII-49 (43)	*M. scheuchzeri*	11.9	0.3	227	13	24.9	< 0.001
306.8	Cottage Coal (roof shale)	FN VIII:178 (20)	*M. scheuchzeri*	13.5	0.9	210	20	27.4	0.5
306.8	Cottage Coal (roof shale)	SI-100 (11)	*M. scheuchzeri*	12.8	0.8	188	31	—	—
306.8	Cottage Coal (floor)	FNIX:85 (7)	*M. scheuchzeri*	15.2	0.6	203	16	25.5	1.7
306.8	Cottage Coal (floor)	FNIX:85 (9)	*N. ovata, var. sarana*	14.5	1.3	235	29	21.7	1.1
306.8	Baker Coal Hymera Coal (roof shale)	38417 (8)	*M. scheuchzeri*	16.0	0.8	251	17	29.7	0.9
306.8	Baker Coal (roof shale)	43518; IL2007-03 (15)	*M. scheuchzeri*	13.2	1.2	225	25	—	—
307.5	Springfield Coal (roof shale)	38317 (4)	*N. ovata, var. acon.*	12.5	0.9	242	21	24.8	0.0
307.5	Springfield Coal (roof shale)	38866; FN1987-5 (11)	*N. ovata, var. sarana*	13.5	0.9	219	21	26.7	0.4

Age (Mya)	Associated Coal	Sample ID [1](stomatal box counts)	Taxa	Stomatal Index		Stomat. Density		Stomat. Length	
				mean	± 2 Std. Err.	mean	± 2 Std. Err.	mean	± 2 Std. Err.
307.5	Springfield Coal (roof shale)	43499; FNIII-118 (8)	*N. ovata, var. acon.*	12.6	0.9	226	11	27.3	0.0
307.5	Springfield Coal (roof shale)	FNVII-82 (12)	*M. scheuchzeri*	13.6	0.7	299	23	27.0	0.0
307.5	Springfield Coal (roof shale)	FNVII-98 (5)	*M. scheuchzeri*	14.9	1.6	192	39	—	—
308.3	Colchester Coal (roof shale)	38355 (4)	*M. scheuchzeri*	9.4	0.6	181	27	19.0	1.1
309.1	Seeleyville Coal (roof shale)	38314 (15)	*M. scheuchzeri*	13.3	0.7	232	11	23.0	0.3
311.4	Murphysboro Coal: FN II-111	FN II-111 (35)	*N. ovata, var. acon.*	11.6	0.4	184	12	22.4	0.4
311.5	Murphysboro(floor)	FN8-114 (55)	*N. ovata, var. acon.*	11.9	0.5	223	10	28.1	0.3
311.5	Murphysboro (floor)	FN II-111-112 (4)	*N. ovata, var. acon.*	13.0	1.3	193	21	28.7	0.0
312.2	Upper Block Rider	FNVII: 65-66 (7)	*M. scheuchzeri*	10.0	0.5	110	4	30.6	0.0

[1]For each count, stomata were measured within a square to rectangular box with a total area of 0.04 mm^2.

[2]Stomatal Index values were calibrated to paleo-pCO_2 using the method of McElwain and Chaloner (*ref.* 49) and three nearest-living equivalents (NLE). The stomatal ratio method[13] applied an average SI of the three NLEs of 18.1 and a Recent calibration. See Methods for more detail.

Stomatal Width		Cuticle $\delta^{13}C_{org}$		Atm. $\delta^{13}C_{carb}$		^{2}SI-based pCO_2		Mechanistic pCO_2		
mean	± 2 Std. Err.	‰	(± 1σ)	‰	range	mean	± 2 Std. Err.	mean	16%	84%
13.5	1.1	-24.8	0.3	-5.8	-0.4/+0.2	495	41	462	322	701
20.2	< 0.001	-24.8	0.3	-5.8	-0.4/+0.2	458	17	421	293	649
13.3	0.4	-24.8	0.3	-5.8	-1.3/+0.6	322	21	393	274	610
12.0	0.7	-25.1	0.3	-6.3	±1.1	475	52	472	331	712
15.6	< 0.001	-26.2	0.3	-6.5	-1.1/+1.4	354	19	507	355	767
17.2	0.8	-26.2	0.3	-6.5	-1.1/+1.5	368	17	446	260	690
9.5	0.3	-26.2	0.3	-6.5	-1.2/+1.4	477	26	582	412	864
13.3	4.8	-25.5	0.3	-5.8	-1.6/+1.1	551	11	477	332	730
14.4	0.4	-24.4	0.3	-5.8	-0.4/+1.4	492	34	480	333	737
—	—	—	—	—	—	473	50	—	—	—
13.3	0.8	-24.4	0.3	-5.8	-0.4/+1.4	429	40	431	307	667
9.0	0.7	-24.4	0.3	-5.8	-0.4/+1.4	458	46	397	277	610
15.4	0.5	-24.5	0.3	-5.8	-0.4/+1.4	409	22	358	247	561
—	—	—	—	—	—	509	50	—	—	—
13.2	0.0	-25.2	0.3	-5.6	-0.4/+1.4	522	35	536	376	805
12.2	0.9	-25.2	0.3	-5.6	-0.4/+1.4	485	30	527	371	795

Stomatal Width		Cuticle $\delta^{13}C_{org}$		Atm. $\delta^{13}C_{carb}$		^{2}SI-based pCO_2		Mechanistic pCO_2		
mean	± 2 Std. Err.	‰	(± 1σ)	‰	range	mean	± 2 Std. Err.	mean	16%	84%
13.6	0.0	-25.2	0.3	-5.6	-0.4/+1.4	548	35	567	401	846
15.5	0.0	-25.2	0.3	-5.6	-0.4/+1.4	487	23	388	266	615
—	—	—	—	—	—	494	72	—	—	—
8.5	0.4	-24.3	0.3	-4.9	-0.9/+1.1	691	41	611	434	898
11.5	0.5	-24.6	0.3	-4.9	-1.2/+0.9	493	27	484	336	734
10.0	0.2	-23.5	0.3	-4.9	-1.2/+0.9	567	18	494	350	735
15.9	0.1	-23.5	0.3	-4.9	-1.2/+0.9	558	24	475	335	712
13.5	0.0	-23.5	0.3	-4.9	-1.2/+0.9	507	64	469	330	703
13.6	0.0	-24.0	0.3	-4.9	-1.2/+0.9	650	32	604	427	881

Supplementary Table 4. Parameter descriptors, data input ranges and scaling factors used to estimate pCO_2 from fossil *Neuropteris ovata* and *Macroneuropteris scheuchzeri*

Input	Description	Range of input values	Reference/Justification/Method
#Dab:	stomatal density (m^2) on abaxial surface	99.34 to 375 mm^2	Measured on fossil cuticles
#eDab	error in Dab in m^2	9.93 to 37.5 mm^2	1σ uncertainty of fossil cuticle measurements
#Dad:	stomatal density (m^2)	0	All fossil species hypostomatous
#eDad:	error in Dad	0	All fossil species hypostomatous
#GCLab:	guard cell length (m) on abaxial surface	17.84 to 37.73 µm	Measured directly from cuticles. Where guard cell length could not be directly measured because stomata were sunken the stomatal pit length was measured. Pit length underestimates guard cell length by approximately 5% (ref. *87*)
#eGCLab:	error in GCLab.	1.7 to 2.02 µm	10% error
#GCLad:	guard cell length (m) on adaxial surface	0	All fossil species hypostomatous
#eGCLad:	error in GCLad.	0	All fossil species hypostomatous
#GCWab:	single guard cell width (m) on abaxial surface	7.98 to 20.21µm	Measured directly from fossils. Where individual guard cells were not visible, the width of both guard cells in a stomatal complex was measured and halved to estimate a single guard cell width.
#eGCWab:	error in #GCWab:	0.07 to 2.02 µm	10% error
#GCWad:	single guard cell width (m) on adaxial surface	0	All fossil species hypostomatous
#eGCWad:	error in #GCWad:	0	All fossil species hypostomatous
#$d^{13}C_p$:	$\delta^{13}C$ of leaf material relative to that in the PDB standard (‰).	-23.49 to -26.19 ‰	Measured directly from from representative leaf fragments of *M. scheuchzeri* and *N. ovata* at each stratigraphic level where SD data were recorded.
#$ed^{13}C_p$:	error in $\delta^{13}p$.	1	Suggested error of ref. *14*
#$d^{13}C_{atm}$:	ratio of $\delta^{13}C$ in paleo-atmosphere relative to that in	-4.9 to -6.5 ‰	Estimated from brachiopod $d^{13}C_{calcite}$ reported in ref. *39* and assuming $\Delta^{13}C$ ($\delta^{13}C_{calcite}$—

	the PDB standard (‰)		$\delta^{13}C_{CO2(g)}$) of 9.22‰ at SST of 23°C (ref. *40*).
#ed$^{13}C_{atm}$:	error in $\delta^{13}Ca$	1	Suggested error (ref. *14*)
#CO_2_0:	atmospheric CO_2 concentration associated with A0 (ppm)	400 ppm	All Ao values of NLEs were measured at 400 ppm CO_2
#A0:	photosynthetic rate at CO_2_0 (µmol/m^2/s).	*M. scheuchzeri*: 16 ± 1 µmol/m^2/s *N. ovata* = 13 ± 1 µmol/m^2/s	Ao values at 400 ppm were estimated as indicated above using a D_V for *M. scheuchzeri* of 3.42 mm/mm^2 and for *N. ovata* of 4.49 mm/mm^2).
#gb:	boundary layer conductance to CO_2 (mol/m^2/s).	2 mol/m^2/s	Suggested value of ref. *14*
#egb:	error in gb.	0.2 mol/m^2/s	10% error which is greater than suggested value of ref. *14*
#s1:	scaling from guard cell length (GCL) to stomatal pore length (Pl).	0.48	Scaling relationship determined by measurements taken from SEM images of *Neuropteris* stomata from ref. *89*. Value = 0.48.
#es1:	error in s1	0.1	2 x suggested error of ref. *14*.
#s2:	scaling from single guard cell width (GCW) to stomatal depth (l).	1	Assumed that *Neuropteris* and *Macroneuropteris* guard cells have a circular cross-section (ref. *14*).
#es2	error in s2.	0.05	Suggested error of ref. *14*
#s3:	scaling from the area of a circle with the diameter of pore length to a_{max} (maximum area of stomatal pore). s3 is equivalent to b in Table S2 of SOM of ref. *14*.	0.6	As in ref. *14*, however N ovata and M. scheuchzeri likely had a low leaf margin area (based on exceptionally thin cuticle) and an angiosperm model would therefore be more appropriate with a scaling of 0.6.
#es3:	error in s3	0.025	
#s4:	scaling from maximum conductance to CO_2 (gcmax) to operational conductance to CO_2 (gcop).	0.2	See Methods for justification
#es4:	error in s4.	0.02	Recommended error of ref. *14*
#s5:	scaling from photosynthetic	0.013	Generic scaling of 0.013 (ref. *14*)

	rate (A) to mesophyll conductance to CO_2 (gm).		
#es5:	error in s5.	0.0065	100X recommended error of ref. *14*

Supplementary Table 5. G_{max} values for various extinct species representative of the simulation groups used in BIOME—BGC v.4.2.

Group	Representative Taxa	G_{max} (mol m^{-2} s^{-1})	Source
Macroneuropteris	*Macroneuropteris scheuchzeri*	1.48	Ref. *51*
other Medullosales (medullosans)	*Alethopteris lesquereuxi*	6.29	Ref. *88*
	A. sullivanti	12.77	Ref. *89*
	Blanzyopteris praedentata	13.37	Ref. *90*
	Laveineopteris loshii	4.88	Ref. *91*
	L. tenuifolia	7.78	Ref. *92*
	Lescuropteris genuina	1.79	Ref. *93*
	Neuralethopteris schlehanii	5.57	Ref. *91*
	Neuropteris aconiensis	0.48	Ref. *94*
	N. britannica	1.74	Ref. *94*
	N. flexuosa	1.80	Ref. *94*
	N. loshii	2.68	Ref. *94*
	N. macrophylla	0.86	Ref. *94*
	N. obliqua	1.89	Ref. *90*
	N. ovata var. *aconiensis*	1.41	Ref. *94*
	N. ovata var. *sarana*	1.13	Ref. *94*
	N. ovata var. *simonii*	1.43	Ref. *94*
	N. rarinervi	2.34	Ref. *94*
	N. subariculata	1.51	Ref. *94*
	N. tenuifolia	4.02	Ref. *94*
	Reticulopteris germarii	4.02	Ref. *95*
	Schopfiastrum decussatum	5.01	Ref. *96*
	Senftenbergia plumosa	0.57	Ref. *97*
Sphenophyllum	*Sphenophyllum apiciserratum*	0.26	Ref. *98*
	S. emarginatum	0.79	Ref. *99*
	S. koboense	0.18	Ref. *98*
	S. miravallis	0.54	Ref. *100*
	S. speciosum	0.30	Ref. *101;* Ref. *102*
Lepidodendrales	*Bothrodendron minutifolium*	2.67	Ref. *103*

(lycopsids)			
	B. punctatum	4.44	Ref. *103*
	Lepidodendron aculeatum	3.53	Ref. *104*
	L. arberi	3.66	Ref. *104*
	L. dichotomum	8.15	Ref. *104-105*
	L. feistmanteli	5.61	Ref. *104*
	L. loricatum	3.79	Ref. *105*
	L. mannabachense	2.22	Ref. *104*
	L. obovatum	4.65	Ref. *105*
	L. peachii	3.60	Ref. *104*
	L. rhodianum	1.23	Ref. *104*
	L. subdichotomum	3.73	Ref. *104*
	L. veltheimii	2.56	Ref. *104*
	Lepidophloios acadianus	2.95	Ref. *106*
	L. acerosus	3.20	Ref. *106*
	L. grangeri	3.28	Ref. *106*
	L. laricinus	5.47	Ref. *106*
	Ulodendron landsburgii	3.44	Ref. *107*
	U. majus	8.3	Ref. *103*
Cordaitales (cordaitaleans)	*Cordaabaxicutis boleslawii*	1.59	Ref. *108*
	C. borassifolioides	4.44	Ref. *108*
	C. brzyskii	12.05	Ref. *108*
	C. czeczottensis	4.65	Ref. *108*
	C. gorae	3.13	Ref. *108*
	C. papilloborassifolius	6.50	Ref. *108*
	C. sierszae	2.21	Ref. *108*
	Cordaadaxicutis bracteatus	0.48	Ref. *108*
	C. carpaticus	0.09	Ref. *108*
	C. janinae	0.11	Ref. *108*
	C. krawjewskae	0.06	Ref. *108*
	C. laziskae	7.38	Ref. *108*
	C. pussilostomatus	0.31	Ref. *108*
	C. tectostomatus	0.06	Ref. *108*
	C. zalezensis	0.16	Ref. *108*
	C. zoldanii	0.31	Ref. *108*
	Cordaites borassifolius	0.14	Ref. *109-110*
	C. pilsensis	0.57	Ref. *109*
	C. principalis	1.99	Ref. *111*
	C. rerichensis	1.62	Ref. *109*
Ferns (mostly marattialean tree ferns)	*Acitheca polymorpha*	0.40	Ref. *112*
	Diplazites unitus	0.07	Ref. *112*
	Lobatopteris aspidioides	1.05	Ref. *112*
	L. miltonii	0.35	Ref. *112*
	L. polypodioides	0.30	Ref. *112*
	Pecopteris cyathea	0.05	Ref. *112*
	P. cf. micromiltonii	0.12	Ref. *112*
	Rumohra adiantiformis	0.07	Ref. *113*
	Sphaeropteris cooperi	0.26	Ref. *114*
	Sydneia manleyi	0.27	Ref. *115*

Supplementary Table 6. Values of C:N and maximum leaf width for representative groups and species of each simulation group.

Group	Median C:N (range)	Species	Leaf width (cm)	Source
Macroneuropteris	21.5 (13—30)	*Macroneuropteris scheuchzeri*	1.5 – 3.0	Ref. *116*
Medullosales	38.5 (35—42)	*Alethopteris* spp.	0.5	Ref. *117*
		Glenopteris splendens	1.2	Ref. *118*
		Medullosa anglica	0.3	Ref. *119*
		Neuropteris attenuata	0.2	Ref. *120*
Sphenophyllum	32 (22—42)	*Sphenophyllum apiciserratum*	0.4-1.2	Ref. *98*
		S. kobense	0.6-1.7	Ref. *98*
		S. meridionale	0.4-0.5	Ref. *98*
		S. minor	0.8-1.6	Ref. *98*
		S. sinocoreanum	0.6-1.5	Ref. *98*
Lepidodendrales (lycopsids)	43 (40—46)	*Lepidodendron aculeatum*	0.4	Ref. *121*
		Lepidoxylon anomalum	0.3-1.0	Ref. *122*
		Lepidophylloides hippocrepicus	0.4	Ref. *123*
Cordaitales	40 (30—50)	*Cordaites grandifolius*	0.6	Ref. *122*
		C. borassifolius	0.5-0.8	Ref. *122*

		C. communis	1.5-3.7	Ref. *122*
		C. diversifolius	1.2-1.5	Ref. *122*
		C. mansfiedli	1.5	Ref. *122*
		C. gracilis	0.5	Ref. *122*
Ferns (mostly marattialean tree ferns)	31 (20—42)	*Corynepteris cabrierensis*	0.2	Ref. *124*
		Alloiopteris erosa	0.2	Ref. *124*
		Pecopteris cf. cyathea	0.3	Ref. *125*
		P. puertollanensis	0.2	Ref. *125*

Supplementary Table 7. Final model parameters for the representative taxonomic groups used in the BIOME—BGC v.4.2 modeling.

Group	**Foliar C:N (kg C kg N^{-1})**	**SLA (m^2 kg C^{-1})**	**G_{max} (mol m^{-2} s^{-1})**	**G_b (mol m^{-2} s^{-1})**
Macroneuropteris	21.5	30.3	1.47	1.71
Medullosales	38.5	24.4	2.64	3.46
Sphenophyllum	32.0	22.0	0.49	2.66
Lepidodendrales	43.0	22.8	3.97	3.69
Cordaitales	40.0	23.9	2.29	2.23
Ferns (mostly marattialean tree ferns)	31.0	36.4	0.42	5.41

Supplementary Table 8. Atmospheric input properties for the BIOME—BGC v.4.2 simulations of this study.

Time (Mya)	[CO2]atm (ppm)	pO_2	P (Pa)	M_a (g mol^{-1})	c_p (J $kg^{-1}K^{-1}$)
299.5	874.08	0.30	115000.0	29.37	990.75
301.0	691.82	0.30	114226.9	29.34	991.64
302.1	210.24	0.30	113578.6	29.30	992.87
304.2	89.58	0.29	112209.2	29.27	994.17
307.6	475.88	0.27	109456.1	29.22	995.93
308.2	948.76	0.27	109116.6	29.23	995.52
325.0	144.38	0.21	100921.9	28.96	1004.58
326.0	1551.45	0.21	100910.3	29.03	1002.45
344.0	385.58	0.23	103451.0	29.05	1001.64

Supplementary Table 9. Modeled areal extent (%) of select biomes on late Paleozoic land surface. All results from ref. *6.* Horizontal color banding differentiates climate stages (I to IV on Supplementary Fig. 8). Minimum and maximum values indicated by white and yellow shading, respectively.

		840 ppm				***560 ppm***			
Stage	**Orbit Interval**	**Wetland Forest**	**Tropical Shrubland /Desert & Barren Land**	**Tundra**	**Taiga**	**Wetland Forest**	**Tropical Shrubland/ Desert & Barren Land**	**Tundra**	**Taiga**
late interglacial	160	22.6%	21.4%	12.4%	14.5%	24.7%	17.9%	17.9%	12.1%
early glacial	165	21.5%	26.4%	3.9%	19.1%	29.8%	22.3%	5.8%	15.6%
early glacial	170	21.4%	28.4%	2.7%	15.1%	29.4%	27.2%	3.9%	11.2%
peak glacial	175	22.4%	25.8%	2.2%	17.1%	30.7%	24.4%	3.2%	13.4%
peak glacial	180	23.3%	21.9%	2.0%	19.3%	30.4%	20.6%	2.7%	16.7%
peak glacial	185	22.8%	25.0%	2.1%	19.6%	29.4%	24.5%	2.7%	15.7%
peak glacial	190	21.2%	27.1%	2.2%	18.8%	28.0%	26.9%	3.1%	15.4%
peak glacial	195	21.0%	26.0%	2.5%	21.5%	28.3%	23.5%	3.7%	17.9%
peak glacial	200	20.9%	25.1%	4.5%	20.0%	27.7%	23.9%	4.6%	17.4%
peak glacial	205	20.8%	26.2%	3.6%	19.8%	28.2%	24.3%	4.4%	17.3%
late glacial	210	21.8%	26.8%	2.3%	19.8%	28.8%	25.4%	3.3%	16.0%
late glacial	215	22.3%	25.9%	2.1%	19.2%	29.3%	23.5%	2.9%	16.2%
late glacial	220	23.7%	22.3%	1.9%	20.1%	29.9%	20.1%	2.3%	18.0%
late glacial	225	22.6%	25.3%	2.2%	20.0%	28.4%	24.9%	2.2%	16.5%
deglaciation	230	21.2%	30.3%	2.1%	16.3%	26.0%	30.8%	2.6%	12.6%
interglacial	235	20.8%	25.4%	2.5%	19.1%	26.1%	23.1%	2.9%	20.3%
Avg. Interglacial		21.5%	25.7%	5.7%	16.6%	25.6%	24.0%	7.8%	15.0%
Avg. early glacial		21.4%	27.4%	3.3%	17.1%	29.6%	24.8%	4.8%	13.4%
Avg. peak glacial		21.8%	25.3%	2.7%	19.4%	29.0%	24.1%	3.5%	16.3%
Avg. late glacial		22.6%	25.1%	2.2%	19.8%	29.1%	23.5%	2.7%	16.7%
Min value		20.8%	21.4%	1.9%	14.5%	24.7%	17.9%	2.2%	11.2%
Max value		23.7%	30.3%	12.4%	21.5%	30.7%	30.8%	17.9%	20.3%
Max change		2.9%	8.9%	10.4%	7.0%	6.0%	12.9%	15.7%	9.1%

		420 ppm				*280 ppm*			
Stage	**Orbit Interval**	**Wetland Forest**	**Tropical Shrubland /Desert & Barren Land**	**Tundra**	**Taiga**	**Wetland Forest**	**Tropical Shrubland/ Desert & Barren Land**	**Tundra**	**Taiga**
late interglacial	160	38.8%	18.4%	10.1%	9.2%	47.1%	21.9%	5.9%	8.1%
early glacial	165	43.3%	21.8%	5.0%	10.4%	49.2%	24.3%	3.6%	8.4%
early glacial	170	41.8%	25.5%	3.6%	8.9%	49.2%	26.1%	3.3%	7.9%
peak glacial	175	43.7%	21.5%	3.8%	9.2%	49.7%	23.5%	3.2%	8.1%
peak glacial	180	43.2%	21.4%	4.2%	9.6%	49.9%	22.5%	3.0%	8.1%
peak glacial	185	44.1%	22.1%	3.4%	9.6%	49.4%	23.7%	3.1%	8.3%
peak glacial	190	43.1%	23.3%	4.1%	9.3%	49.7%	24.2%	3.2%	8.4%
peak glacial	195	42.7%	23.1%	4.5%	9.6%	49.2%	23.5%	4.0%	9.0%
peak glacial	200	43.1%	22.8%	5.6%	9.5%	48.9%	23.2%	4.5%	8.5%
peak glacial	205	44.0%	21.8%	4.9%	9.2%	49.1%	24.1%	4.3%	8.5%
late glacial	210	44.6%	23.1%	3.8%	8.7%	49.6%	24.3%	3.4%	8.9%
late glacial	215	45.6%	21.1%	3.6%	8.5%	49.5%	23.9%	3.2%	8.4%
late glacial	220	45.1%	20.5%	3.5%	8.9%	48.6%	22.7%	3.1%	8.4%
late glacial	225	45.4%	21.4%	3.4%	8.7%	49.2%	24.7%	3.5%	7.7%
deglaciation	230	44.7%	24.5%	2.9%	7.5%	48.9%	26.0%	3.3%	7.6%
interglacial	235	44.6%	21.2%	4.3%	8.6%	50.1%	22.8%	3.8%	7.8%
Avg. Interglacial		42.7%	21.4%	5.8%	8.4%	48.7%	23.4%	4.3%	7.8%
Avg. early glacial		42.6%	23.6%	4.3%	9.6%	49.2%	25.2%	3.5%	8.2%
Avg. peak glacial		43.4%	22.4%	4.4%	9.4%	49.4%	23.5%	3.6%	8.4%
Avg. late glacial		45.2%	21.5%	3.6%	8.7%	49.2%	23.9%	3.3%	8.4%
Min value		38.8%	18.4%	2.9%	7.5%	47.1%	21.9%	3.0%	7.6%
Max value		45.6%	25.5%	10.1%	10.4%	50.1%	26.1%	5.9%	9.0%
Max change		6.7%	7.1%	7.2%	2.9%	3.0%	4.2%	2.9%	1.5%